1

Radiation processes and models

JULIEN MALZAC

Abstract

This is a basic introduction to the physics of compact objects in the context of High Time Resolution Astrophysics (HTRA). The main mechanisms of energy release and the properties of relevant radiation processes are briefly reviewed. As a specific example, the top models for the multi-wavelength variability of accreting black holes are unveiled.

1.1 Introduction

Compact objects represent a prime target for HTRA. Their physics involves strong gravitational fields, matter compressed to enormous densities, very high energy particles and huge magnetic fields. Of course, such extreme conditions cannot be produced in a laboratory on Earth. In many cases, high time resolution observations of theses objects represent a unique opportunity to test fundamental theories regarding particle interactions, the properties of dense matter or gravitation. Compact objects also inform us on fundamental astrophysical processes such as accretion and ejection in their most extreme form.

Classically there are three types of compact objects that all form mostly (but not only) through the gravitational collapse of a normal star after exhaustion of its thermonuclear fuel. White Dwarfs (hereafter WDs) have masses lower than the Chandrasekhar limit (1.4 $M_\odot$) and a radius comparable to that of the Earth. The quantum degeneracy pressure of the electrons balances the gravitation forces to prevent collapse. Neutron Stars (hereafter NSs) are instead supported by short-range repulsive neutron-neutron interactions mediated by the strong force and also by the quantum degeneracy pressure of neutrons. They can have masses up to the Tolman-Oppenheimer-

Volkoff (TOV) limit which is approximately between 2–3 $M_\odot$. Above the TOV limit a star cannot support its own weight.[1] It is completely collapsed and forms a Black Hole (hereafter BH). The size of a NS is about 10 km, the size of a BH is given by the size of the horizon of events. The latter depends on the spin of the BH but remains comparable to the gravitational radius: $R_g = GM_{\rm BH}/c^2 \simeq 1.5\, M_{BH}/M_\odot$ km. A typical stellar mass BH concentrates about 10 times the mass of the sun within a radius of about 15 km. This corresponds to an average density within R_g of about $10^{15}\,{\rm g\,cm^{-3}}$. The average density of the matter of a NS is of the same order i.e. 10^{14} times denser than planet Earth! The surface gravity on a NS is more than 10^{11} times that on Earth. The dynamical time-scale in the environment of compact objects are very short. For example the period of a Keplerian orbit at 6 times the radius of the object corresponds, on Earth, to a geosynchronous orbit: it has a period of exactly one day. This time-scale is reduced to a few minutes around a WD and only a few milliseconds around a NS or a BH ! Compact objects can also release tremendous amounts of energy in their environment in the form of radiation and powerful outflows. This is this combination of power and very short dynamical time-scales makes compact objects one of the main target of HTRA. Section 1.2 presents the basic mechanisms of energy release around compact objects through dissipation of gravitational, magnetic and rotational power. Then, in Section 1.3, the main emission processes responsible for the conversion of fraction of this energy into photons are described. Finally, Sections 1.4 and 1.5 focus on models for the multi-wavelength variability of accreting black hole in X-ray binary systems involving respectively the accretion flow and the jets.

1.2 Compact objects

Energy can be extracted from the rotation of the compact object (Pulsars), its magnetic field (magnetar), from the gravitational energy of material falling onto the compact object (accretion in binary systems) or even Thermonuclear fusion of outer layers of accreted materials (X-ray bursters, classical novae). In this section I briefly introduce the different mechanisms of energy release. A much more detailed exposition of compact objects physics can be found in classical textbooks, such as those by Shapiro and Teukolsky (1983); Frank et al. (1992); Longair (1994); Kato et al. (2008). There are also many excellent reviews covering specific recent developments of the field,

[1] Note that objects supported by the quantum degeneracy pressure of quarks, and named quark stars, have also been theorised and would have properties very similar to that of neutron stars, but their existence is disputed.

for instance Patruno and Watts (2012) on millisecond X-ray pulsars, Watts (2012) on thermonuclear burst oscillations, Gilfanov and Sunyaev (2014) on the structure of the boundary layer in accreting neutron stars, (Smith, 2006) on Cataclysmic variables, or Done et al. (2007) on accreting BHs and NSs...

1.2.1 Rotation

All stars are rotating (the rotation period of the sun is about 27 d). In the case of NSs and BHs the angular momentum is essentially conserved during the gravitational collapse. The compactification of the star then implies faster rotation. As a result a newborn neutron star can have a spin period P of the order of $P = 10$–100 ms. On the other hand, most WDs have slow rotation due removal of angular momentum during the loss of the progenitor's outer envelope in a planetary nebulae. Nevertheless a WD can later be spun-up by accretion (see Section 1.2.3). The fastest spinning WD has a period of only $P = 13$ s (Mereghetti et al., 2011). The rotational energy of a star can be estimated simply as $E_{\rm rot} = I\Omega^2/2 = 2I\pi^2 P^{-2}$ where I is the moment of inertia which, for a homogeneous sphere of mass M and radius R is $I = 2MR^2/5$. For a NS this energy can represent a small but significant fraction of the rest mass energy of the star:

$$\frac{E_{\rm rot}}{Mc^2} \simeq 10^{-4} \left(\frac{R}{10\,{\rm km}}\right)^2 \left(\frac{P}{0.01\,{\rm s}}\right)^{-2}, \tag{1.1}$$

In absolute terms the rotation energy of a young neutron star is comparable to the energy radiated by the sun during 1 billion years. However, this energy is released over much smaller time-scales of the order of 10^3 to 10^7 yr. Indeed, the extraction of rotational energy implies spin-down. The rotational power is related to the spin-down rate as

$$\dot{E}_{\rm rot} = \frac{d}{dt}\left(\frac{I\Omega}{2}\right) = 4I\pi^2\frac{\dot{P}}{P^3} \simeq 3{\times}10^{50}\frac{M}{M_\odot}\left(\frac{R}{10\,{\rm km}}\right)^2\left(\frac{P}{0.01\,{\rm s}}\right)^{-2}\frac{\dot{P}}{P} \quad {\rm erg\,s^{-1}}. \tag{1.2}$$

The 'braking' time-scale over which the rotation power is released can be estimated as $E_{\rm rot}/\dot{E}_{\rm rot} \sim P/\dot{P}$. Pulsars are NSs emitting beams of radiation leading to the highly coherent modulation of the observed light curve at the spin period. In these sources both the spin and spin down rate can be measured accurately (see Chapter 5 by A. Possenti in these proceedings) and this allows one to estimate the released rotation power. In the case of the Crab pulsar the observed period is $P \simeq 33$ ms and spin-down rate is $\dot{P}/P \simeq$

$10^{-11}\,\mathrm{s}^{-1}$ which leads to $\dot{E}_{\rm rot} \simeq 10^{38}$ erg s^{-1}. This power is comparable to the accumulated radiative output of about 10^5 stars like the Sun. This power is larger than the observed luminosity of the source but comparable to the power required to feed the surrounding pulsar wind nebula. This coincidence indicates that the pulsar wind is powered by the rotational energy of the pulsar.

The rotational power is extracted via the effects of the strong magnetic field of the neutron star. Indeed, during the gravitational collapse leading to the formation of the NS, the conservation of magnetic flux across the stellar surface implies that the magnetic filed is amplified by a factor $\sim R_\star^2/R^2$, where $R_\star$ is the initial radius of the star and R is the radius of the compact object. For a star of the size of the sun compacted into a 10 km radius, this amplification factor is of order of 5×10^9 ! As a result the typical surface magnetic field of a young neutron star is of the order of 10^{11}-10^{12} G. For comparison, the Earth magnetic field is $\sim 0.5\,\mathrm{G}$, a fridge magnet is $\sim 50\,\mathrm{G}$, the strongest continuous field yet produced in a laboratory is about 5×10^5 G. Because of the high conductivity of the NS matter, its magnetic field dissipates only very slowly, on times scales much longer than the 'braking' time-scale of the NS. In practice it can be considered a constant. The young NS therefore behaves has a huge spinning magnet. It is known from electromagnetic theory that a magnetic dipole rotating in vacuum radiates. The radiated energy can be estimated simply as

$$\dot{E}_d = \frac{B_p^2 R^6 \Omega^4}{6c^3} \sin^2\alpha \simeq 10^{39} \left(\frac{B_p}{10^{12}\,\mathrm{G}}\right)^2 \left(\frac{R}{10\,\mathrm{km}}\right)^6 \left(\frac{P}{0.01\,\mathrm{s}}\right)^{-4} \sin^2\alpha \quad \mathrm{ergs}^{-1}, \tag{1.3}$$

where B_p is the magnetic field amplitude at the poles of the compact star and α is the misalignment angle between the direction of the dipole and the spin of the neutron star. This radiated power can be matched to the observed rotational power in pulsars in order to estimate the pulsar magnetic field, its age etc... But in reality the magnet is not spinning in vacuum. Huge electric fields are generated close to the surface of the NS. Those fields extract charged particles from the NS. These charged particles distribute themselves around the star to neutralise the electric field: an extended magnetosphere is formed. Streams of charged particles leave the star at high latitudes where the magnetic field lines are open, leading to the formation of a wind. The rotation energy is dissipated mostly through the interaction of the magnetic field of the NS with the magnetosphere and the wind. Nevertheless the

energy losses remain comparable to that predicted by the simple magnetic dipole radiation model.

1.2.2 Magnetic field dissipation

Some NSs appear to have negligible rotation energy but huge magnetic fields up to 10^{14}-10^{16} G. These strongly magnetised NSs define the class of Magnetars (see e.g. Woods and Thompson, 2006). It has been shown (Thompson and Duncan, 1993) that such magnetic fields may have built up through dynamo processes (similar to that generating the Earth or the sun magnetic fields) during the first moments of the life of the NS. This strong dynamo amplification occurs only if the NS is formed with a spin period $P < 5$ ms. After 10–30 s, the core has cooled down and is not hot enough for efficient dynamo. The magnetic braking is very efficient and the rotation energy is dissipated very quickly. After few minutes the rotation has slowed down to a period of a few seconds. But the magnetic fields remain so strong that they can push and move material around in the star interior and crust. This leads to large amounts of magnetic dissipation during the first 10^4 y. Magnetic dissipation in the interior of the star keeps the star hot and bright producing mostly X-ray thermal emission. Magnetic dissipation may also occurs in the surrounding magnetosphere due to twisting of the magnetic field lines and reconnection (similar to solar corona). This can lead to bursts of non-thermal X-ray and gamma-ray radiation which are observed in sources called 'soft gamma-ray repeaters'.

1.2.3 Accretion

Accretion is the growth of a massive object by gravitationally attracting more matter. This is an ubiquitous astrophysical process leading to the formation of planets, stars, galaxies and the growth of super-massive BHs. The gravitational energy released during accretion onto super-massive BHs also appears to regulate the joint growth of the BHs and their host galaxy. Accretion onto stellar compact objects can be observed if the compact objects is in a binary system and can accrete gas from its companion star. As this type of accretion occurs in bright nearby sources evolving on human time-scales it is relatively easy to observe and study, and some of the knowledge gained may be extrapolated to other accreting systems such as super-massive BHs in Active Galactic Nuclei (AGN). As will be discussed below accretion onto a compact star in an accreting binary system depends on the nature of the donor star (high mass vs low mass star). It depends also on the nature of

the compact star. Gas accreting onto a NS or a WD will ultimately hit the hard surface of the star. This has observable effects such as the presence of a boundary layer in which the gas is stopped, or the triggering of nuclear explosions (X-ray bursts in NS, classical novae in WD) when enough material has been accreted onto the surface. The structure of the accretion flow may also be affected by the strong magnetic field of the star as is the case for NS in X-ray pulsars or WD in polars. Such complications do not occur in accreting BHs where we can observe accretion in its 'purest' form: as the gas crosses the event horizon without notable effects, all the observed radiation must originate from the accretion flow.

Accretion power

Accreting matter falls into the potential wells of a compact object and loses gravitational energy. For accretion to occur gravitational energy (and angular momentum) must be dissipated away, mostly in form of radiation. If accretion occurs at a mass accretion rate $\dot{M}$ onto an object of size R and mass M the gravitational power that is dissipated is given by the gravitational potential on the surface

$$\dot{E}_{\rm ac} = \dot{M}\frac{GM}{R} = \eta\dot{M}c^2, \tag{1.4}$$

where $\eta = GM/Rc^2$ is called the accretion efficiency. It represents the amount of energy released per unit of mass energy accreted. The accretion efficiency onto a WD is of the order of 10^{-4} while accretion onto a neutron star reaches 0.1. Due to the absence of a hard surface when accreting onto a BH, the efficiency depends on the structure of the accretion flow. For thin accretion discs (see below) the accretion efficiency is in the range 0.057–0.42 depending on the BH spin. For comparison accretion onto planet Earth has $\eta \sim 10^{-9}$, while the Sun has $\eta \sim 10^{-6}$. The efficiency of thermonuclear fusion of hydrogen is $7{\times}10^{-3}$. Accretion onto a compact object is therefore much more efficient than fusion at releasing energy.

Eddington limit

The accretion power is however limited by the amount of matter that we are able to accrete. There is a fundamental limit on the mass accretion rate that is set by the Eddington luminosity. The Eddington luminosity is the maximum luminosity for which the gravitational force on a fluid element exceeds the radiation pressure (i.e. the maximum luminosity at which matter can be accreted). Let us consider a fluid element of mass m located at a distance d from the center of the compact object which radiates isotropically

a luminosity L. The amplitude of the force of gravity is $F_{\rm grav} = GMm/d^2$. The radiation pressure force is proportional to the local radiation flux and is directed in opposite direction. It is given by $F_{\rm rad} = L\kappa m/(4\pi\, d^2 c)$, where the opacity κ is a measure of the effectiveness of the transfer of momentum from radiation to the fluid element. Since both forces are proportional to m/d^2. The condition for equilibrium $F_{\rm grav} = F_{\rm rad}$ is independent of both the mass and distance of the fluid element. This condition defines the Eddington luminosity

$$L_{\rm E} = \frac{4\pi GMc}{\kappa} \simeq 1.46 \times 10^{38} \frac{M}{M_\odot} \quad {\rm ergs}^{-1}. \tag{1.5}$$

The accreting gas is usually hot and ionised, so that the opacity is dominated by electron scattering. In this case $\kappa = \kappa_{es} = 0.34$ cm^2 g^{-1} for standard abundances. This is the value of κ that was assumed in the numerical estimate given in equation 1.5. This immediately implies a maximum accretion rate

$$\dot{M}_{\rm E} = L_{\rm E}/\eta c^2 = 2.6 \times 10^{-9}\, (M/M_\odot)\, \eta^{-1} \quad M_\odot\, {\rm yr}^{-1} \tag{1.6}$$

For a compact object with a hard surface (NS or WD), the Eddington mass accretion rate depends only on its size

$$\dot{M}_{\rm E} = \frac{4\pi cR}{\kappa} = 1.8 \times 10^{-8} \left(\frac{R}{10\,{\rm km}}\right) \quad M_\odot\, {\rm yr}^{-1} \tag{1.7}$$

This maximum luminosity and accretion rate are estimated for a spherical accretion geometry and radiation field, and deviation from spherical are of course expected to occur and may allow to exceed somewhat the Eddington limit (which indeed appears to be violated in some sources). Nevertheless this gives a good estimate of the maximum power that can be extracted through accretion onto a compact object. This power is huge. The Eddington luminosity of a $10\, M_\odot$ BH is comparable to the combined luminosity of 10^6 stars like the Sun.

Mass transfer

However there is another limitation related to the capacity of the compact object to attract and capture gas from the donor star. This is the so-called mass transfer problem. Before falling onto the compact object the gas must escape the pull of the donor star. The effective gravitational potential in a binary system is determined by the masses of the stars and the centrifugal force arising from the motion of the two stars around one another. One may

write this potential as a function of r_1 and r_2 the distance to the center of each star and r_3 the distance to the rotation axis

$$\phi = -\frac{GM_1}{r_1} - \frac{GM_2}{r_2} - \frac{\Omega_{\rm orb}^2 r_3^2}{2}, \tag{1.8}$$

where $\Omega_{\rm orb}$ is the orbital angular velocity. The equipotential surfaces form two lobes surrounding each of the stars that are called the Roche lobes. The two lobes are connected through a point called the first Lagrangian point (or L1) where the sum of the centrifugal and gravitational forces vanishes. This is a saddle point in the potential which forms a pass that the gas from the donor has to climb before being able to fall into the influence of the compact object.

Roche lobe overflow Mass transfer may occur simply if the donor fills its Roche lobe. This may result from an increase of the stellar radius during the evolution of the star. This can also be driven by changes in the orbital parameters that make the Roche lobe smaller. This can also occur occur through loss of angular momentum (by emission of gravitational waves, magnetic braking, tidal torques, mass loss in a stellar wind...). Also mass transfer, over time, will change the mass ratio of the two components and affect the orbital parameters. So even if the donor fills its Roche lobe, accretion may be instable and may not be sustained. It can be shown that stable lobe overflow can occur only if the mass of the donor is smaller than the mass of the accretor. If these two conditions are fulfilled then steady mass accretion occurs at rates of the order of $\dot{M} \sim 10^{-10}$–10^{-9}. Such systems are called low-mass X-ray binaries (hereafter LMXB).

Wind accretion A massive early type companion (O or B) can loose mass in a wind at a rate 10^{-6}–10^{-5} $M_\odot$ yr^{-1} and supersonic velocity comparable to the escape velocity of the star

$$v_{\rm w} \sim v_{\rm esc} = \sqrt{\frac{2GM_\star}{R_\star}} \sim 10^3 \quad {\rm km\,s^{-1}} \tag{1.9}$$

The compact star will gravitationally capture matter from a roughly cylindrical region with axis along the relative wind direction. This cylinder represents the volume where the wind particle kinetic energy is less than the gravitational potential (e.g. Bondi and Hoyle, 1944; Bondi, 1952; Davidson and Ostriker, 1973; Lamb et al., 1973; Frank et al., 1992). The radius of the

cylinder, called the accretion radius or gravitational capture radius, is given by

$$r_{\rm acc} \simeq \frac{2GM}{v_{\rm rel}^2 + c_{\rm s}^2} \tag{1.10}$$

where $c_{\rm s}$ is the sound speed in wind, $v_{\rm rel}^2 = v_{\rm orb}^2 + v_{\rm w}^2$, and v_{orb} is the orbital velocity of the gas.
The net amount of gas captured and accreted by the compact object can be obtained by combining this relationship with Kepler's third law and the continuity equation (assuming spherically symmetric and steady mass loss)

$$\dot{M} = \pi r_{\rm acc}^2 \rho v_{\rm rel} \sim (10^{-5} - 10^{-4})\dot{M}_{\rm w} \sim 10^{-11} - 10^{-9} M_\odot \,{\rm yr}^{-1} \tag{1.11}$$

We can see that both wind accretion in HMXB an Roche lobe overflow in LMXB allow mass transfer at a rate that is smaller than, and yet a significant fraction of, the Eddington limit.

Keplerian accretion discs

Once the material is captured, it would orbit the compact object indefinitely unless it can get rid of its angular momentum and be accreted. It is viscosity, and the associated viscous torques between annuli in the disc, that allows angular momentum to be transferred outwards and mass to spiral inwards. Any original ring of particles will thus spread out into a disc, with the outer radius being determined by tidal torques from the companion. However, ordinary molecular viscosity is completely inadequate to account for the observed properties of discs and some kind of turbulent viscosity is invoked. The best candidate as the origin of this turbulent viscosity is the Magneto-rotational instability which develops in differentially rotating flows and can generate fully developed Magneto-HydroDynamic (MHD) turbulence that provides efficient angular momentum transport (Balbus and Hawley, 1991, 1998). The characteristic scale of the turbulence must be less than the disc thickness, H, and the characteristic turbulent speed is expected to be less than the speed of sound, $c_{\rm s}$, since there is no strong evidence for turbulent shocks. The viscosity, ν, is therefore often parametrised by writing it as $\nu = \alpha c_{\rm s} H$, placing all the uncertainties in the unknown parameter α, taken to be less than 1. This is the standard alpha-disc model of accretion discs (Shakura and Sunyaev, 1973). This model also assumes that radiation cooling in the disc is very efficient. All the locally dissipated accretion power is radiated away on the spot in the form of blackbody radiation. As a consequence the disc is cold and geometrically thin. From these two assumptions,

it is possible to determine analytically the full disc structure as a function of the distance r from the compact object. Although there is still no reliable way of calculating α, it turns out that the observable properties of a steady accretion disc are largely independent of α. In particular the total luminosity of the disc is simply half of the gravitational power at the disc inner radius R_i, $L_{\rm disc} = 2GM\dot{M}/R_i$. Most of the luminosity comes from the inner part of the accretion flow, 80 % of the power is radiated within $10R_i$. The temperature profile in the disc is

$$T(R) = T_0 \left(\frac{R_i}{r}\right)^{3/4} \left(1 - \sqrt{\frac{R_i}{r}}\right)^{1/4}, \tag{1.12}$$

where

$$T_0 = \left(\frac{3GM\dot{M}}{8\pi\sigma R_i^3}\right)^{1/4} \simeq 6 \times 10^7 \left(\frac{R_i}{R_G}\right)^{-3/4} \left(\frac{\dot{M}c^2}{L_E}\right)^{1/4} \left(\frac{M}{M_\odot}\right)^{-1/4} \quad \text{K}. \tag{1.13}$$

The temperature has a maximum around $3R_i$ and then decreases with the distance like $r^{-3/4}$. This maximum temperature can reach a few keVs in NSs and BHs. The innermost and most luminous part of the accretion disc will therefore produce mostly X-ray radiation. The spectral energy distribution (SED) of the whole accretion disc is constituted of the sum of all the blackbodies emitted at different radii in the disc with a different temperatures. Longer wavelengths allow one to probe more distant regions of the accretion flow. We note the standard Shakura-Sunyaev disc model assumes pure Newtonian physics, the general relativistic version of the thin disk model was introduced by Novikov and Thorne (1973).

Hot accretion flows

The thin accretion disc model assumes full energy thermalisation and this implies a low temperature, a high density and a small disc scale height $H/R \sim 10^{-3}$–10^{-4}. If instead, the disc is hot, then the gas pressure makes the scale height larger $\simeq 0.1$–0.5 and this reduces the density. As a consequence the radiation cooling is less efficient and a high temperature can be maintained. Indeed, the density becomes so small that the collision timescales between electrons an ions of the plasma can be long compared to the accretion time-scale. Then the protons acquire most of the gravitational energy through viscous heating but this energy can only be radiated efficiently by the electrons. Since electrons and protons are decoupled, the

two populations end up having very different temperatures. The protons can reach $\sim 10^{12}$ K while the electrons are much colder (and yet very hot), $\sim 10^{9}$ K in the innermost part of the accretion flow. In this kind of hot accretion flow the accretion energy is not radiated away locally, it can be carried inward with the flow until it is swallowed by the BH or hit the surface of the compact star. These advection dominated accretion flows (Ichimaru 1977; Narayan & Yi 1994) produce mostly non-thermal Comptonised radiation (see Section 1.3.4). Hot accretion flows have been extensively studied. Analytic solutions have been found taking also into account the effects of convection; convection dominated accretion flows (CDAF, Narayan et al., 2000) and outflows; advection dominated inflow-outflow solution) (ADIOS, Blandford and Begelman, 1999). Hot accretion flow have also been found in numerical simulations (Stone et al., 1999).

Jet launching from accretion flows

Accreting NS and BH (an perhaps also WD) can launch highly collimated jets of magnetised plasma that travel at near light speed, carrying away a significant fraction of the accretion power (Mirabel and Rodríguez, 1994; Fender and Gallo, 2014). These jets propagate over large distances and can have an enormous impact on the surrounding medium over distance scales that are far out of the gravitational reach of the BH itself. The details of the formation of those jets are unclear, none of the models and simulations take into account all the physics. But all models require magnetic fields. The mechanism proposed by Blandford and Payne (1982) involves magnetic field lines threading the accretion disc. Provided that the magnetic field lines are are sufficiently inclined with respect to the disc, the centrifugal force can throw away some of the accreting material, which remains tied to the rotating magnetic field lines like a bead on a wire. Then the jet needs to somewhat collimate and this requires large scale coherent magnetic field structures. Another mechanism involves electromagnetic extraction of energy from a Kerr BH. Indeed, Penrose (1969) and Christodoulou (1970) have shown that up to 30 % of the mass energy of a maximally spinning BH can be theoretically extracted. Then, Blandford and Znajek (1977) have shown that an accretion disc can allow this energy to be extracted and drive powerful jets. The magnetic field carried by the accreted gas remain threaded through the BH horizon. The frame of the field lines is dragged along with the rotation of the BH. These rotating field lines induce an electromagnetic force that accelerates charged plasma at relativistic speeds along the axis of rotation. Due to the radial component of the field, the particles spiral as they leave.

Effects of the magnetic field of a compact star on the accretion flow

Magnetic fields become dynamically important close to the compact object at a distance called the Alfven radius, $R_{\rm a}$. At $R_{\rm a}$ the magnetic energy is comparable to the kinetic energy of the infalling gas: $\rho v^2/2 \simeq B^2/8\pi$. For the purpose of simple estimates, we can assume that the accreting gas is in free fall in a spherical geometry, so that $v \simeq v_{\rm ff} = \sqrt{2GM/R_{\rm a}}$ and $\rho = \dot{M}/(4\pi R_{\rm a}^2 v_{\rm ff})$. Assuming a dipole magnetic field around a WD or NS of radius $R_\star$: $B(R_{\rm a}) \sim B_p\, R_\star^3/R_a^3$, we then obtain

$$R_{\rm a} \simeq 30\,{\rm km} \left(\frac{B_p}{10^9\,G}\right)^{\frac{4}{7}} \left(\frac{\dot{M}}{2\times10^{-8}\,M_\odot\,{\rm yr}^{-1}}\right)^{-\frac{2}{7}} \left(\frac{M}{M_\odot}\right)^{-\frac{1}{7}} \left(\frac{R_\star}{10\,{\rm km}}\right)^{\frac{12}{7}}. \tag{1.14}$$

The effects of the magnetic field are important only if $R_a > R_\star$, which translates into the following condition for the surface magnetic field:

$$B_p > 1.5\times10^8 \left(\frac{\dot{M}}{2\times10^{-8}\,M_\odot\,{\rm yr}^{-1}}\right)^{\frac{1}{2}} \left(\frac{M}{M_\odot}\right)^{\frac{1}{4}} \left(\frac{R_\star}{10\,{\rm km}}\right)^{-\frac{5}{4}} \quad {\rm G}. \tag{1.15}$$

As discussed above in Sections 1.2.1 and 1.2.2, in the case of NS this condition will be easily verified and the magnetic fields of the star will interfere with the accretion process. At $R_{\rm a}$ the magnetic field can force accreting material in co-rotation with the compact star. If the spin period of the compact star is longer than the orbital period at $R_{\rm a}$, the centrifugal forces cannot balance gravity anymore and the material flows along magnetic field lines onto the magnetic poles of the compact star. This forms an X-ray pulsar if the compact star is a NS, and a polar in the case of a WD. The magnetic field transfers angular momentum from the accretion flow to the compact star exerting an effective spin up torque on the star. If the spin period of the compact star is shorter than the orbital period at $R_{\rm a}$, the corotation implies that the centrifugal forces overcome gravity: accretion is stopped. This is the so called propeller regime, in which angular momentum is transported from the compact star to the 'accretion' flow. In this case the magnetic field exerts a spin-down torque on the star. The spin of the compact star therefore evolves through propeller and accreting regimes to reach an equilibrium in which the spin period of the star is equals to the orbital period at $R_{\rm a}$

$$P_{\rm eq} \simeq 3\,{\rm ms}\left(\frac{B_p}{10^9\,G}\right)^{\frac{6}{7}}\left(\frac{\dot{M}}{2\times10^{-8}\,M_\odot\,{\rm yr}^{-1}}\right)^{-\frac{3}{7}}\left(\frac{M}{M_\odot}\right)^{-\frac{5}{7}}\left(\frac{R_\star}{10\,{\rm km}}\right)^{\frac{18}{7}}. \tag{1.16}$$

This equation shows that accretion will spin up a NS up to spins of a few ms. Such sources are observed, these are the millisecond X-ray pulsars (Wijnands and van der Klis, 1998; Harding, 2013; Tauris, 2015).

Compact stars with weak magnetic field: boundary layer

Many compact stars appear to have a magnetic field below the threshold defined by equation 1.15. Indeed, accretion seems to cause dissipation of the magnetic field which may be considerably reduced in the course of the history of the accreting compact star. In this case the accretion disc can extend undisturbed very close to the surface of the star. There is however a region between the accretion flow and the star where the accreting gas has to decelerate from the orbital velocity to the rotation velocity of the star, spinning up the compact star in the process. This region is called the boundary layer (BL). Since most of the kinetic energy of the gas is dissipated in the BL the luminosity of the BL is comparable to the total luminosity of the accretion disc: $L_{\rm BL} \sim \dot{M}\,v_{\rm K}^2/2 = GM\dot{M}/(2R_\star) \sim L_{\rm disc}$. Matter has a significant latitude velocity component in the boundary layer, spreading above the compact star surface and decelerating due to friction (like a wind above the sea, Inogamov and Sunyaev (1999). For sources with luminosity greater than 5 % Eddington, the local radiation flux is Eddington. In this regime the spreading layer temperature is independent of luminosity. Emission models predicts a temperature of the order of 2.5 keV which was confirmed by observations. The size of the belt must increase with accretion rate/luminosity. For $L \sim L_{\rm E}$, the spreading layer covers the whole surface of the compact star (Gilfanov and Sunyaev, 2014).

1.3 Radiation processes

From radio waves to gamma-rays, compact objects radiate over the whole electromagnetic spectrum. This radiation can be emitted through thermal radiation (i.e. blackbody emission related to the temperature of the object) or non-thermal processes like Synchrotron or inverse Compton. Synchrotron radiation is produced by very energetic charged particles spiralling around magnetic field lines. Relativistic particles accelerated in shocks in the jets produce synchrotron emission mostly in the radio, sub-mm and infrared (IR)

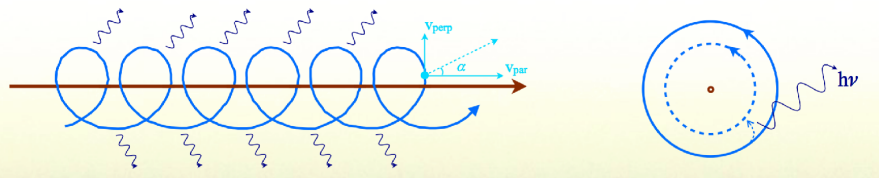

Figure 1.1 Emission of an electron spiralling in a magnetic field

bands. A similar process, called curvature radiation, is related to the propagation of particles along very curved field lines. It can be important in the magnetosphere of neutron stars. An accretion flow can be very hot and contains energetic electrons of temperature up to a billion K. It also contains many low energy photons produced by synchrotron radiation or coming from the outer regions of the accretion flow. These photons collide with the hot electrons and gain energy at each interaction. This process is called Inverse Compton scattering. If the photon can make several interactions before escaping the hot gas, the process is called Comptonisation. It leads to the production of hard X-ray radiation. Inverse Compton from relativistic particles in the jets may also produce gamma-rays. Understanding the radiation processes allows one to extract the information that is encoded in the radiation received from these objects. It enables to measure many physical parameters of the system such as temperatures, velocities, magnetic fields, the energy of accelerated particles and their distribution. It also helps to determine the size and geometry of the emitting regions and test the predictions of theoretical models. By simultaneously observing in different bands we learn about the joint evolution of the different components of the systems (e.g. accretion flow and jets). In this section, I summarize the main properties of the cyclo-synchrotron, curvature radiation, Bremsstrahlung, inverse Compton and photon-photon pair production. A more detailed discussion of these radiation processes can be found in classical text books such as those by (Rybicki and Lightman, 1986; Longair, 1992; Jackson, 1999).

1.3.1 Cyclo-Synchrotron

Cyclo-synchrotron radiation is the radiation produced by a charged particle accelerated by the magnetic field. In the following I consider an e^- which gyrates around the magnetic field lines with a velocity v (see Figure 1.1). The component of its velocity which is parallel to the magnetic field is a constant. The transverse component of the velocity has a constant modulus

and a direction that is rotating uniformly around the magnetic filed line. The constant angle α between the velocity and the magnetic field is called the pitch angle. The rotation frequency $\nu_B = \nu_{\rm L}/\gamma$, where $\gamma = \left(1 - v^2/c^2\right)^{-1/2}$ is the Lorentz factor of the particle and $\nu_{\rm L} = qB/2\pi m_e c = 2.8 \times 10^6\,{\rm B\,Hz}$, is the Larmor frequency. The magnetic field B is expressed in G. The radius of the 'orbit' around the magnetic field is given by the Larmor radius: $r_L = p_\perp c/(2\pi\nu_{\rm L}) = 1.7{\times}10^3 p_\perp/B$ cm, where $p_\perp = p\sin\alpha = \gamma v \sin\alpha/c$. Because the particle has a transverse acceleration it radiates. The cyclo-synchrotron emission is calculated under a number of assumptions. First, the magnetic field must be uniform at the Larmor scale. This implies for instance that there is no turbulence at that scale. The magnetic field lines must not be too curved as this can be the case in the magnetosphere of pulsars for example. Moreover, as the particle radiates, its kinetic energy and Larmor radius both decrease. The energy loss must be small on the a giration time-scale, in other words we require that the cooling time-scale the particle $t_{\rm cool} >> 1/\nu_{\rm B}$. Finally we will present the results obtained in the classical limit in which the magnetic field is smaller than the critical limit $B_{\rm c} = m_e c^3/\hbar q = 4.4. \times 10^{13}\,{\rm G}$. Above this limit the particle energies and orbits around the magnetic field become quantised.

Power

The radiated power of an accelerated particle is given by the Larmor formula

$$P = \frac{2q^2}{3c^3}\gamma^4\left(a_\perp^2 + \gamma^2 a_\parallel\right), \tag{1.17}$$

where $a_\perp$ and $a_\parallel$ represent the component of the acceleration that are perpendicular and parallel to the velocity respectively. In the case of particle girating in the magnetic field $a_\parallel = 0$ and $a_\perp = \nu_{\rm B}\, v_\perp/2\pi$. The radiated power can be written as $P = 2c\sigma_{\rm T}\, U_{\rm B}\, p_\perp^2$, where $U_{\rm B} = B^2/8\pi$ is the magnetic field energy density, and $\sigma_{\rm T}$ is the Thomson cross section (see Section 1.3.4). Usually the distribution of pitch angles is isotropic. This is either because the distribution of radiating particles is isotropic, or the magnetic field is isotropically tangled, or both. Then the average over the pitch angles gives

$$P = \frac{4}{3}c\sigma_T U_{\rm B} p^2. \tag{1.18}$$

Therefore the requirement that the cooling time of a particle $t_{\rm cool} \simeq \gamma m_{\rm e} c^2/P$ is longer than the giration time-scale $1/\nu_{\rm B}$, implies a limit on the product of the particle energy and magnetic field

$$\gamma^2 B < 2q/r_0^2. \tag{1.19}$$

Optically thin synchrotron spectrum

If the charged particle moves very slowly around the magnetic field lines, the amplitude of the electric field measured at large distance is proportional to the sine of the angle between the acceleration vector and the direction to the observer. This angle changes with time t as the particle 'orbits' the magnetic field and the observer observes a sinusoidal modulation of the electric field: $E(t) = \sin 2\pi\nu_{\rm B} t$. The emitted spectrum is proportional to the Fourier power spectrum of the fluctuations of the electric field which, in this case is a Dirac delta function. In other words, the observer sees a line at frequency $\nu_{\rm B}$. If the particle is moving faster, the emission pattern is modified by Doppler beaming and harmonics appear in the spectrum. For a relativistic particle, the emission is beamed within an angle $1/\gamma$ around the direction of the velocity. When this emission cone crosses the direction to the observer, she measures a briefly increased electric field. The duration of this pulse is $\delta t \simeq 1/(\nu_{\rm B}\gamma^3)$[2]. This pulsed modulation of the electric field at frequency ν_B is made of multiple lines at frequencies that are multiple of ν_B and extending up to a frequency $\nu_{\rm c}$ that is comparable to the time scale of the pulse:

$$\nu_{\rm c} = \frac{3}{2}\gamma^3 \nu_B \sin\alpha. \tag{1.20}$$

In the ultra-relativistic case ($\gamma >> 1$), ν_B vanishes and the spectrum tends toward a continuum. This limit is called Synchrotron emission, while the non-relativistic case is called cyclotron emission. In fact once one consider not only the emission from a unique particle but that of a set of particles with different directions of propagation and pitch angles the harmonic lines are considerably broadened, even in the mildly-relativistic case (see Marcowith and Malzac 2003 for a general calculation of this case).

Equation. 1.18 shows that the emission increases quadratically with the momentum of the particle, the radiation induced by the magnetic fields will be more likely to be important in the Synchrotron regime which is therefore the most relevant for the observations. In this limit, the shape of the spectrum radiated by a relativistic particle is given by Rybicki and Lightman (1986)

[2] The line of sight remains in the emission cone during $1/(\nu_{\rm B}\gamma)$, the additional γ^{-2} factor is caused by photon travel time effects.

$$\frac{dP}{d\nu}(\alpha, p, \nu) \;=\; \frac{\sqrt{3}q^3 B}{m_e c^2} \sin\alpha F\left(\frac{\nu}{\nu_{\rm c}}\right), \tag{1.21}$$

where

$$F(x) \;=\; x\int_x^\infty K_{5/3}(z)dz, \tag{1.22}$$

and $K_n(z)$ is the modified Bessel function of second kind. Then the pitch angle averaged spectrum can be approximated as

$$\frac{dP}{d\nu}(\gamma, \nu) \;=\; \frac{12\sqrt{3}\sigma_{\rm T} c U_{\rm B}}{\nu_{\rm L}} \sin\alpha G\left(\frac{\nu}{2\nu_{\rm c}^*}\right), \tag{1.23}$$

where

$$G(x) \;=\; x^2\left[K_{4/3}(x)K_{1/3}(x) - \frac{3x}{5}\left(K_{4/3}^2(x) - K_{1/3}^2(x)\right)\right]. \tag{1.24}$$

In both cases, the spectrum increases with frequency $\frac{dP}{d\nu} \propto \nu^{1/3}$ up to the critical frequency ν_c, (or $\nu_c^* = \frac{3}{2}\nu_{\rm L}\gamma^2$ in the angle averaged case), where there is a turn-over and an exponential cut-off. The emission is therefore peaked around the critical frequency, and both ν_c and ν_c^* scale like $B\gamma^2$. The condition of slow particle energy losses, given by equation 1.19, then implies a maximum frequency at which synchrotron emission can be produced. The particles cannot radiate synchrotron emission above this energy because they cool before closing a full orbit. This maximum frequency depends only on fundamental constants and is independent of the magnetic field or particle energy: $h\nu_{\rm max} = 3\,mc^2/\alpha_f = 70\,{\rm MeV}$. Any emission above 70 MeV cannot be due to synchrotron.

Of course in real situations the radiating particles are not mono-energetic but have a distribution in energy. One common case is a relativistic Maxwelian distribution: $N(\gamma) \propto \gamma\sqrt{\gamma^2-1}e^{-\gamma/\theta}$, where θ is the reduced temperature: $\theta = kT/m_e\,c^2$. In this case the spectrum peaks at $h\nu = 1.5\,h\nu_{\rm L}\theta^2$, at lower frequencies the emitted spectrum is $\frac{dP}{d\nu} \propto \nu^{1/3}$ and an exponential a cut-off at higher energies. Another interesting case corresponds to a power-law particle energy distribution $N(\gamma) \propto \gamma^{-s}$, in the range $\gamma_{\rm min} < \gamma < \gamma_{\rm max}$. Then the emitted spectrum is $\frac{dP}{d\nu} \propto \nu^{1/3}$ up to $\nu = 1.5\,\nu_{\rm L}\gamma_{\rm min}^2$ where the photon spectral slopes changes to $\alpha = (s-1)/2$, ($\frac{dP}{d\nu} \propto \nu^{-\alpha}$) until it reaches a high frequency cut-off at $\nu = 1.5\,\nu_{\rm L}\gamma_{\rm max}^2$.

Synchrotron self-absorption

From the point of view of the electron, the emission of cyclo-synchrotron emission constitutes a spontaneous transition between energy levels. As in the case of atomic transitions, the spontaneous emission mechanisms coexist with the opposite transition which happens through absorption of radiation. The transition probabilities are described by the Einstein coefficients and their relations. On can show (see e.g. Ghisellini and Svensson (1991) that the absorption coefficient (in cm^{-1}) can be expressed as a function of the emissivity $j_\nu = \int_1^\infty \frac{N(\gamma)}{4\pi}\frac{dP}{d\nu}d\gamma$ (erg $\mathrm{s}^{-1}\,\mathrm{Hz}^{-1}\,\mathrm{cm}^{-3}\,\mathrm{ster}^{-1}$):

$$\alpha_\nu = \frac{1}{2m_e\nu^2}\frac{1}{p\gamma}\frac{d\gamma p j_\nu}{d\gamma}. \tag{1.25}$$

where α_ν gives the probability for photon travelling in the magnetised plasma to be absorbed per unit of distance crossed. The specific intensity I_ν (erg $\mathrm{s}^{-1}\,\mathrm{Hz}^{-1}\,\mathrm{cm}^{-2}\,\mathrm{ster}^{-1}$) of the synchrotron radiation escaping a homogeneous medium of size L is given by the resolution of the radiative transfert equation

$$I_\nu = \frac{j_\nu}{\alpha_\nu}\left(1 - e^{-\tau_{\mathrm{sa}}}\right), \tag{1.26}$$

where $\tau_{\mathrm{sa}} = \alpha_\nu L$ is the Synchrotron self-absorption optical depth. There are two main assymptotic regimes depending on the value of τ_{sa}. For $\tau_{\mathrm{sa}} << 1$ the medium is optically thin: $I_\nu \simeq j_\nu L$ while for $\tau_{\mathrm{sa}} >> 1$ the medium is optically thick and he synchrotron emission is self-absorbed: $I_\nu = j_\nu/\alpha_\nu$. As τ_{sa} decreases with photon frequency, the low frequency part of the spectrum is usually self-absorbed, while at higher frequency the emission is optically thin. The transition between optically thin and thick emission occurs at a frequency ν_{t} such that by $\tau_{\mathrm{sa}}(\nu_{\mathrm{t}}) \simeq 1$. The value of ν_{t} increases with electron density (or Thomson depth $\tau_{\mathrm{T}} = n_{\mathrm{e}}\,\sigma_{\mathrm{T}}\,L$). The exact value of the turnover frequency as well as the shape of the spectrum in the self-absorbed regime depends on the shape of the electron energy distribution. For a thermal distribution the low frequency self-absorbed part of the spectrum is a black body in the Rayleigh-Jeans regime i.e. $I_\nu \propto \nu^2$. For a powerlaw energy distribution the turnover frequency can be estimated analytically $\nu_{\mathrm{t}} \propto B^{\frac{s+2}{s+4}}\tau_T^{\frac{2}{s+4}}$ and the low frequency self-absorbed spectrum is strongly inverted: $I_\nu \propto \nu^{5/2}$.

1.3.2 Curvature radiation

Curvature radiation is emitted by relativistic particles moving along strongly curved magnetic field lines. This process is important in the magnetosphere of pulsars where the field lines are curved and the magnetic field is so strong that the transverse component of the velocity is radiated very quickly and then the particles just follow very closely the magnetic field lines. In this case the acceleration is perpendicular to the fields lines and the emission is beamed in the direction of the trajectory. The observer sees a pulse every time the line of sight intercepts the beam of radiation traveling with a nearly circular motion along the magnetic field lines. This situation is in fact equivalent to synchrotron emission. The radiated power and spectrum for one particle is therefore given by the same formulae as for synchrotron with the Larmor frequency replaced by the rotation frequency of the relativistic particles $\nu_{\rm L} = c/2\pi R$, where R is the curvature radius of the field lines. The mono-energetic spectrum of curvature radiation has therefore the same form as that of synchrotron radiation. It varies like the cube root of frequency at low frequencies and falls exponentially above the peak frequency $\nu \simeq 1.5\,\gamma^2\,c/2\pi R$. Then the full observed spectrum depends on the energy and spatial distribution of the particles and magnetic fields in the pulsar magnetosphere. However, for likely values of the parameters, it turns out that the intensity produced by the incoherent sum of a single-particle curvature radiation is not enough to explain the very high brightness temperatures of the radio emission of pulsars. It is necessary to assume that there are charged bunches containing $N \sim 10^{15}$ electrons traveling together at the same velocity and concentrated in a same volume of dimension smaller than the emitted wavelength. Then, these electrons behave as a unique particle of charge qN. Since according to the Larmor formula the radiated power scales like the square of the charge of the particle (equation 1.17), the emission is amplified by a factor N with respect to the sum of the individual emission of the N particle. This amplification is due to the fact that the N electrons radiate in coherence. Such coherence effects may be responsible for the observed emission from the magnetosphere of pulsars.

1.3.3 Bremsstrahlung

Bremsstrahlung is a radiation associated to the acceleration (or in this case braking) of a free electron interacting with the electric field of an ion. The ion is at rest and the electron, which travels with a velocity v, is deflected. This deflection is associated with a transverse acceleration and a distant

observer sees a pulse of electric field. The duration of the pulse is of the order of the duration of the interaction $\Delta t_{\rm int} \simeq b/v$, where b is the impact factor (i.e. the shortest distance at which the electron approaches the ion). The photon spectrum is given by the power spectrum of the pulse which, in the case of random incoherent pulses, is flat up to the cut-off frequency $\nu_{\rm cut} \simeq (2\Delta t_{\rm int})^{-1}$ and exponentially cut-off above that. The amplitude of the flat part of the spectrum for one particle is

$$I_\nu = \frac{8Z^2e^6}{3\pi c^3 m_e^2 v^2 b^2}. \tag{1.27}$$

In a realistic situation we have to integrate this result not only on the energy distribution of the electrons but also on the distribution of their impact factors, since intensity and maximum energy of the spectrum for one particle both diverge when b vanishes, an artificial minimum impact factor has to be assumed. This minimum impact factor can be estimated based on physical arguments, but the full answer requires a quantum physic treatment which introduces correction factors known as gaunt factors. the most common situation is the case of maxwellian electron energy distribution of temperature T. Assuming a fully ionised hydrogen plasma, the Bremsstrahlung emissivity is $j_\nu \propto n_{\rm e} n_{\rm p} T^{-1/2} \exp(-h\nu/kT)$. The emitted spectrum is therefore flat up to a frequency corresponding to a photon energy comparable to the thermal energy of the electrons. The total power represents a cooling term for the plasma

$$J(T) \simeq 2.4 \times 10^{-27} \bar{g}_{ff}(T) n_{\rm e} n_{\rm p} \sqrt{T} \quad {\rm erg\,s^{-1}\,cm^{-3}}, \tag{1.28}$$

where $\bar{g}_{ff}(T)$ is a gaunt factor of the order of unity. Since the radiated power is proportional to square of the plasma number density, Bremsstrahlung will be a very efficient cooling mechanism for dense plasma, and much less efficient for diluted plasmas. In a way that is very similar to cyclo-synchrotron radiation, Bremsstrahlung emission can be self-absorbed. For a thermal plasma, the emission is Rayleigh-Jeans ($I_\nu \propto \nu^2$) below the turn over frequency.

1.3.4 Compton

Compton scattering plays an important role in the formation of the high energy emission of compact objects. In most elementary physics textbooks, it is described as the scattering of a photon by an electron at rest. This results for the photon in a change of direction of propagation and loss of

energy to the electron. In the context of high energy astrophysics the electron can be energetic and moving at relativistic speeds. In this case the electron can transfer a significant amount of energy to the photon which may be up-scattered into the X-ray or even γ-ray domain. This process is then called inverse Compton. It is however exactly the same process as the usual Compton diffusion but considered in a different reference frame. The conservation of momentum and energy during the collision gives the general formula for the change of energy for the photon

$$\frac{\nu'}{\nu} = \frac{1-\mu\beta}{1-\mu'\beta+(h\nu/\gamma m_e c^2)\,(1-\cos\alpha)}, \tag{1.29}$$

where $\beta = v/c$ is the velocity of the electron as a fraction of the speed of light, μ and μ' are the cosine of the angle between the directions of the electron and photon momenta respectively before and after the interaction, ν and ν' are the photon frequencies respectively before and after the collision, α is the angle between the photon directions before and after interaction. If the photon is scattered by an electron at rest this formula simplifies to the classic formula for Compton exchange

$$\frac{\nu'}{\nu} = \frac{1}{1+(h\nu/m_e c^2)\,(1-\cos\alpha)}. \tag{1.30}$$

The photon looses energy in the process (electron recoil effect). If the initial photon energy is small ($h\nu << m_e c^2$)

$$\frac{\Delta\nu}{\nu} = -\frac{h\nu}{mec^2}(1-\cos\alpha). \tag{1.31}$$

If on the contrary, the electron is moving fast, the change in photon energy can be seen as a Doppler effect caused by the change of reference frame. In the electron rest frame the frequency of the incident photon is

$$\nu_o = \gamma\nu(1-\mu\beta), \tag{1.32}$$

and if $h\nu_o << m_e c^2$, the change of photon energy in this frame is negligible $\nu'_o = \nu_o$. Then going back to the lab frame, one gets

$$\nu' = \frac{\nu'_o}{\gamma(1-\mu'\beta)} = \frac{\nu_o}{\gamma(1-\mu'\beta)} = \nu\frac{1-\mu\beta}{1-\mu'\beta}. \tag{1.33}$$

The maximum energy gain is obtained for a frontal collision with back scattering of the photon.

Cross section

The number of scattering events per unit time and unit volume in the lab frame, for a mono-energetic beam of electrons interacting with a mono-energetic beam of photon is

$$\frac{dn}{dt} = n_e n_\nu \sigma_{KN} c\,(1-\beta\mu)\,, \tag{1.34}$$

where n_e and n_ν are the respective electron and photon densities and β the reduced speed of the electrons and μ the cosine of the angle between the two beams, as above. σ_{KN} is the Klein-Nishina the cross section

$$\sigma_{KN} = \frac{2\pi r_e^2}{x}\left[\left(1-\frac{4}{x}-\frac{8}{x^2}\right)\ln(1+x)+\frac{8}{x}-\frac{1}{2(1+x)^2}+\frac{1}{2}\right], \tag{1.35}$$

where x

$$x = \frac{2h\nu}{m_e c^2}\gamma(1-\mu\beta). \tag{1.36}$$

and $r_e = e^2/m_e\,c^2$ is the classical electron radius. In the non-relativistic limit ($x << 1$), the Klein-Nishina cross-section reduces to the Thomson cross-section: $\sigma_{KN} \simeq 8\pi\, r_e^2/3 = \sigma_T$. This non-relativistic limit corresponds to the Thomson regime. Around x$\sim$ 1 the cross section starts to decrease with increasing x, in the ultra-relativistic regime: $x >> 1$, the cross section decreases as

$$\sigma_{KN} \simeq \frac{3}{8}\frac{\sigma_T}{x}\left[1+2\ln(1+x)\right]. \tag{1.37}$$

This strong reduction makes inverse Compton highly inefficient in the Klein-Nishina regime. Finally, the Compton cross section scales like $m_{\rm e}^{-2}$. The scattering cross section on charged particles other than an electron or positron are therefore smaller by a factor of at least $(m_{\rm e}/m_{\rm p})^2 \sim 10^{-7}$. These processes are therefore completely negligible.

Radiated power and amplification

In the Thomson regime ($\gamma h\nu << m_e c^2$) and neglecting the recoil effect ($p^2 >> h\nu/m_e c^2$) the total power radiated by one electron in the field of soft photons of energy density $U_{\rm ph}$ is (Rybicki and Lightman, 1986):

$$P = \frac{4}{3}\sigma_{\rm T} c p^2 U_{\rm ph}, \tag{1.38}$$

where $p = \gamma\beta$ is the reduced momentum of the electron and $U_{\rm ph}$ is the energy density of the target photon field. It is interesting to note that the radiated power in this limit is independent of the actual energy of the soft photons (which do not have to be mono-energetic), or their spectrum.
From equation 1.38 and 1.34, the average photon energy amplification in the course of one interaction is given by

$$\frac{\langle\nu'\rangle}{\nu} = 1 + \frac{4}{3}p^2. \tag{1.39}$$

Spectrum from single scattering of a power-law energy distribution of relativistic electrons

Let us consider an isotropic distribution of photons of typical energy ν_0, scattering off a power-law energy distribution of electrons (i.e. $N(\gamma) = N_0\gamma^{-s}$ in the range $\gamma_{\rm min} < \gamma < \gamma_{\rm max}$), in the Thomson regime. After interaction with an electron of momentum p, the photons have an average energy: $\nu = \nu_0(1+4p^2/3) \simeq \nu_0\, 4\,\gamma^2/3$. As a first approximation we can neglect the dispersion of the scattered photon energies and assume that all the power radiated by the electrons of energy γ is emitted at the average scattered photon energy ν. The emitted spectrum ($\rm erg\,s^{-1}\,Hz^{-1}\,cm^{-3}$) is then

$$j_\nu(\nu) = \frac{4}{3}\sigma_{\rm T}cp^2U_{\rm ph}N(\gamma)\frac{d\gamma}{d\nu} \simeq \frac{2}{3}\sigma_{\rm T}cU_{\rm ph}\frac{N_0}{\nu_0}\left(\frac{3\nu}{4\nu_0}\right)^{-\left(\frac{s-1}{2}\right)}, \tag{1.40}$$

for ν comprised between $\nu_{\rm min} \simeq 4\nu_0\gamma_{\rm min}^2/3$ and $\nu_{\rm max} \simeq 4\nu_0\gamma_{\rm max}^2/3$. The result is therefore a power-law ($j_\nu \propto \nu^{-\alpha}$) extending up to ν_{max} with a slope $\alpha = (s-1)/2$ which is identical to that obtained in the case of synchrotron radiation. If instead, the electrons at γ_{max} emit in the Klein-Nishina regime, the maximum energy of the Compton radiation is limited by the energy of the electrons $h\nu_{\rm max} = \gamma_{\rm max}m_ec^2$. However due to the sharp decrease of the cross section in the KN regime the spectrum deviates from a power-law and is strongly suppressed at photon frequencies that are above $\nu_{\rm KN} \simeq m_e^2c^4/(h^2\nu_0)$.

Multiple Compton Scattering: Thermal Comptonisation

In a realistic situations the photons can undergo zero, one, or several successive scattering before escaping from the energetic electron cloud. In the Thomson regime the probability of interaction is determined by the Thomson optical depth: $\tau_{\rm T} = n_e\sigma_T R$, where n_e is the electron number density and R is the typical dimension of the medium. The probability for a photon to cross the medium without scattering any electron is $\exp(-\tau_{\rm T})$. In

the optically thin case ($\tau_{\rm T} < 1$), and $\tau_{\rm T}$ represent the average number of scatterings before escape (or, in other words its probability of interaction). For $\tau_{\rm T} > 1$ the photons interact at least once and the average number of scattering before escape is $\sim \tau_{\rm T}^2$. Multiple Compton scattering implies non-negligible optical depth, and since the emitting region in compact objects is necessarily small, this also imply a significant density. If the density is large, most of the particles are thermalised. So the most relevant case in which multiple Compton scattering is important is the case of soft photons up-scattered in a hot thermal plasma of electrons (i.e. the electrons have a Maxwellian energy distribution). This process is called thermal Comptonisation. The Comptonized emission depends not only on the Thomson depth but also on the temperature T_e of the electrons. As long as the photon energy $h\nu$ is smaller than the typical energy of the electrons $\sim kT_e$, the photons gain energy at each interaction. In the Thomson limit the average fractional energy gain can be approximated as

$$\frac{\Delta\nu}{\nu} = 4\theta_{\rm e} + 16\theta_{\rm e}^2, \tag{1.41}$$

where $\theta = kT_{\rm e}/m_{\rm e}c^2$ (Rybicki and Lightman, 1986).
Usually one defines the Compton y parameter as the product of this average fractional energy exchange times the average number of interaction:

$$y \simeq \left(4\theta + 16\theta^2\right)\left(\tau_{\rm T} + \tau_{\rm T}^2\right). \tag{1.42}$$

Then one can show that the energy of the incident photon is amplified by a factor

$$A \simeq e^y \left[1 + (e^y - 1)\,\frac{h\nu_0}{m_e c^2}\left(4\theta + 16\theta^2\right)^{-1}\right]^{-1}. \tag{1.43}$$

In the limit of small y, the amplification factor reduces to $A \simeq 1 + y$. While in the limit of large y, the Comptonisation process is said to be saturated and most of the radiation is emitted at an energy $\sim (4\theta + 16\theta^2)m_{\rm e}c^2$, that is comparable to average energy of the electrons.
The escaping spectrum is constituted of the sum of contributions from the photons that have escaped without interaction, plus those that have interacted once before escaping, plus those that have interacted twice, trice...etc. Each of these spectral components, which are called 'Compton orders', forms a broad hump. The average photon energy of each hump increases with the number of interactions until it becomes comparable to the thermal energy

of the electrons. These humps are however apparent in the spectrum only in the optically thin regime $\tau_{\rm T} << 1$. In practice, the observed $\tau_{\rm T}$ are often of the order of unity or larger. In this case the Compton orders are too close and too blended to be individually distinguishable. They combine to form power-law spectrum extending from the typical energy of the seed photons up to the energy of the thermal electrons (Sunyaev and Titarchuk, 1980). At higher energies the spectrum drops-off exponentially. The photon index Γ (defined as $F_\nu \propto \nu^{1-\Gamma}$) can be approximated as

$$\Gamma \simeq C(A-1)^{\delta}, \tag{1.44}$$

with $C \simeq 2.33$ and $\delta \simeq 1/6$ depending weakly on the temperature of the electrons, the average energy of the seed photons and the exact geometry of the comptonizing plasma (Beloborodov, 1999). For instance, for electron temperatures in the range 50–200 keV as mostly observed in X-ray binaries, and for a black body seed photons of temperature $kT_{bb} = 0.15$ keV, numerical simulations give $C = 2.19$, $\delta = 2/15$ (Malzac et al., 2001).
By modelling observed Comptonized spectra it is possible to infer the temperature of the electrons and the Thomson depth. Note that the X-ray spectral slope Γ depends on both parameters (mostly via y). There is therefore a degeneracy which can be broken only if one observe simultaneously at higher energies and measure the Comptonisation cut-off which is usually found around 100 keV (see Section 1.4).

1.4 Model for the accretion flow

Accreting BHs in X-ray binary systems (hereafter BHBs) produce strongly variable radiation over the whole electromagnetic spectrum. From the radio to IR band, non-thermal emission is often detected and usually associated to synchrotron emission from very high energy particles accelerated in jets (see e.g. Chaty et al. 2003, hereafter C03; Gandhi et al. 2011, hereafter G11). The same particles can occasionally produce detectable emission in the GeV range (Fermi LAT Collaboration et al., 2009; Tavani et al., 2009; Malyshev et al., 2013). The thermal emission from the accretion disc can be studied in the optical to soft X-ray bands. In the hard X-ray domain (above a few keV) the emission is dominated by a non-thermal component which nature and origin is strongly debated, and which is associated to the emission of a hot and tenuous plasma located in the direct environment of the BH. This plasma is generically called the 'corona', drawing analogy from the solar corona, although the formation of the BH corona, its power feeding

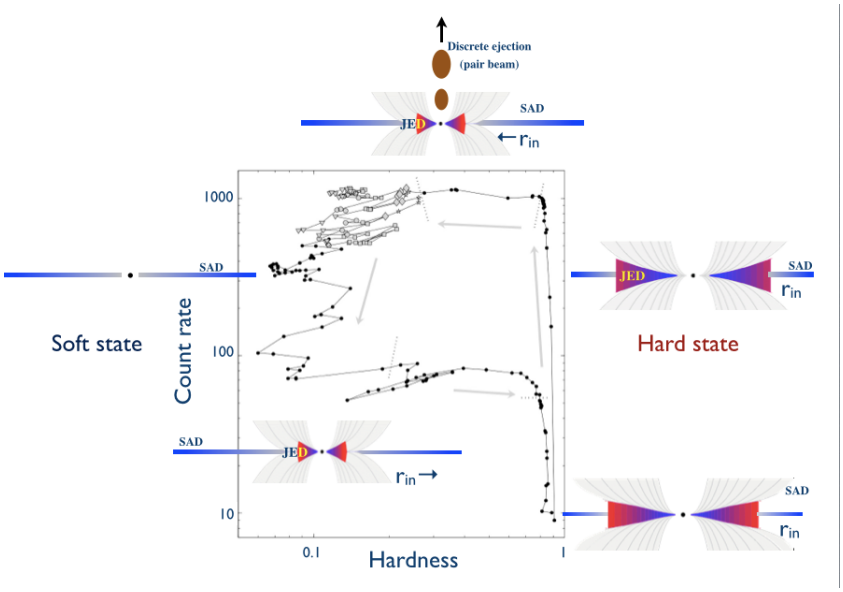

Figure 1.2 Typical track followed by the BHB GX 339–4 in the HID diagram during an outburst. The various sketches illustrate a possible scenario for the evolution of the geometry of the accretion flow in the context of a truncated disc model in which the central hot accretion flow takes the form of a jet emitting disc (Courtesy: P.O Petrucci).

and emission processes are most likely very different from that of the Sun. BHBs also show strong aperiodic and quasi-periodic time variability down to the millisecond scale in X-rays, optical, and IR bands (see e.g. Gandhi et al. 2010, 2008 herafter C10 and G08 respectively). They constitute prime targets for HTRA.

Most BHBs are transient X-ray sources detected during outbursts lasting from a few months to a few years. During outbursts their luminosity can increase by many orders of magnitude to reach values close to the Eddington limit ($L_{\rm E} \simeq 10^{39}\,{\rm erg/s}$ for a $10\,M_{\odot}$ BH), before going down, back to quiescence. These sources therefore constitute a unique laboratory to investigate how the physics of the accretion and ejection depends on the mass accretion rate onto the BH. During these outbursts, not only the luminosity, but also the broad band spectral shape changes drastically as a source evolves through a succession of X-ray spectral states, showing very different spectral and timing properties. Nevertheless those X-ray spectral states can all be described in terms of the same spectral components arising from the thermal accretion disc, X-ray corona and jets. Their rich timing phenomenology (see Chapter 4 by T. Belloni in these proceedings) is poorly understood. In this

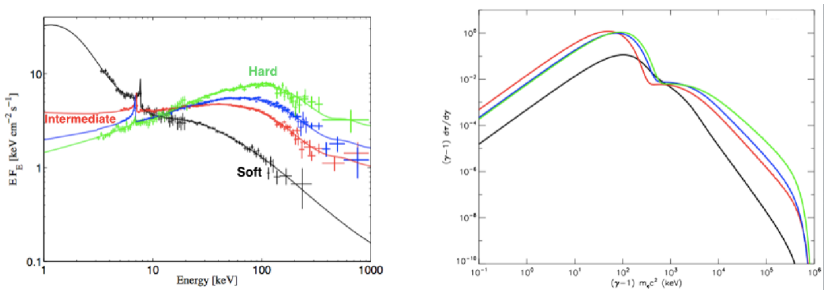

Figure 1.3 Left: Joint INTEGRAL/JEM-X, IBIS and SPI energy spectra of Cyg X–1 during four different spectral states fitted with the magnetised hybrid thermal-non-thermal Comptonisation model BELM. Right: Energy distribution of the Comptonizing electrons obtained in the best fit models of the left-hand side panel. These fits set an upper limit on the amplitude of the magnetic field in the X-ray corona at about 10^5 G in the harder states and 10^7 G in softer states (Del Santo et al., 2013).

section I will focus on a model that can explain qualitatively most of the timing and spectral feature arising from the accretion flow.

1.4.1 Spectral states

The spectral evolution during outburst is usually studied using Hardness Intensity Diagrams (HID). One of such diagrams is shown in Figure 1.2. There are two main stable spectral states, namely the soft and the hard state, corresponding respectively to the left and right hand side vertical branches of the HID (see Figure 1.2). The other spectral states are mostly short-lived intermediate states associated to transitions between the two main spectral states. Some X-ray spectra of Cyg X–1 in its soft (in black), hard (green) and intermediate (blue and red) states are shown in Figure 1.3.

The soft spectral state is observed at luminosity levels ranging approximately from 10^{-2} to a few $0.1L_{\rm E}$. In this state the high energy emission is dominated by the soft thermal multi-blackbody disc emission peaking around 1 keV, for this reason this state is also called 'thermal dominant' by some authors (Remillard and McClintock, 2006). The intense thermal radiation and hot disc temperature ($\sim$ 1 keV) is consistent with that of a standard geometrically thin, optically thick accretion disc (Shakura and Sunyaev, 1973) extending down very close to the BH. The coronal emission is usually very weak forming a non-thermal power-law tail above a few keV. The geometry of the corona is unconstrained in this state but it is generally assumed to be constituted of small-scale magnetically active regions located

above and below the accretion disc (Galeev et al., 1979). In these regions the energetic electrons of the plasma up-scatter the soft X-ray photons coming from the disc into the hard X-ray domain. Due to the weakness of the non-thermal features, the soft state is perfect to test accretion disc models and measure the parameters of the inner accretion disc. In particular the detailed model fitting of the thermal emission of the accretion disc indicates that the inner radius of the disc is a constant and is independent of the luminosity of the system (Gierliński and Done, 2004). This constant inner radius is believed to be located at the innermost stable circular orbit (ISCO) that is predicted by the theory of general relativity and below which the accreting material must fall very quickly across the event horizon. As the size of the ISCO is very sensitive to the spin of the BH this offers an opportunity to constrain the spin of BHs in X-ray binaries. This may also be used to validate the spin measurements made using the relativistic iron K_α line profile which remain the only method that can be used in AGN. This is a difficult task because measuring the disc inner radius accurately requires very detailed disc emission models taking into account the general relativistic effects as well as non-blackbody effects through detailed disc atmosphere models (Davis et al., 2005, 2006). This method also requires the knowledge of the distance and inclination of the system. Nevertheless the most recent BHBs spin estimates obtained from disc continuum and line fitting are converging (see Middleton (2016) for a recent review of these issues). Although the soft state is associated to strong Fe absorption lines indicative of a disc wind (Ponti et al., 2014), there is no evidence so far of any relativistic jet component in soft state (see Russell et al., 2011).

The hard state is observed at all luminosities up to a few 0.1 L_E. In this state the emission from the accretion disc is much weaker and barely detected, the inferred temperature of the inner disc is also lower ($T_{\rm in} \sim 0.1\,$keV) than in soft state state (Cabanac et al., 2009; Dunn et al., 2011; Plant et al., 2015). The X-ray emission is dominated by a hard power-law with photon index Γ in the range 1.5–2.1, and a high energy cut-off around 50–200 keV. This kind of spectra is very well represented by Thermal Comptonisation models with Thomson depth 1-3 and electron temperatures in the range 20–200 keV. In addition there is evidence for a Compton reflection component: the illumination of the thin accretion disc by the Comptonized radiation lead to the formation of a broad hump peaking around 30 keV in the high energy spectrum and a prominent line around 6.4 keV caused by iron fluorescence ($\rm F_e\ K_\alpha$) line. The amplitude R of the reflection component is defined relatively to the reflection produced by an isotropic X-ray source above an infinite slab. In the hard state, R is usually small, $R < 0.3$. Another char-

acteristic of the hard ste is the presence of radio emission with a flat of weakly inverted spectrum that is the signature of steady compact jets. Such compact jets are probably the most common form of jets in X-ray binaries, they appear to be present in all BH and NS binaries when in the hard X-ray spectral state. Their SED extends from the radio to the mid-IR (e.g. Fender et al. (2000), Corbel and Fender (2002); hereafter C03, (Migliari et al., 2010).

The measurements of the hard state X-ray spectrum put interesting contraints on the geometry of the corona in the hard state. For instance, an isotropic corona made of active regions located above the disc (as that envisioned for the soft state) would produce significantly stronger reflection features ($R \sim 1$) which may also be enhanced by general relativistic light bending (Miniutti and Fabian, 2004). In addition, most of the illuminating radiation would be absorbed in the disc (typical disc X-ray albedo is ~ 0.1) and re-emitted at lower energy in the form of nearly thermal radiation. This geometry would thus imply a strong thermal component with an observed flux that would be at least comparable to that of the corona. If the corona has a significant Thomson depth, as inferred by the observations ($\tau_{\rm T} \geq 1$) and is radially extended above the disc, the reflection and reprocessing features might be smeared out by Compton scattering (Petrucci et al., 2001). However detailed Monte-Carlo simulations have shown that in this case the strong reprocessed emission from the disc illuminating the corona would then cool down its electrons (via inverse Compton) to temperatures that are much smaller than observed (Haardt and Maraschi, 1993; Haardt et al., 1994; Stern et al., 1995; Malzac et al., 2001) and then much steeper X-ray spectra would be observed. In fact, the high electron temperature and weakness of the reflection/and disc features suggest that the corona and the disc see each other with a small solid angle.

In this context, a geometry that is favoured is that of the truncated disc model, where the accretion disc does not extend down to the ISCO, but is truncated at some larger distance from the BH. As the disc does not extend deeply into the gravitational potential of the BH, its temperature is lower. As a consequence the blackbody emission is much weaker than in soft state. The corona is constituted of a hot geometrically thick accretion flow that fills the inner hole of the accretion disc (Esin et al., 1997; Poutanen et al., 1997). This hot flow Comptonises the soft photons from the disc and/or internally generated synchrotron photons to produce the hard X-ray continuum. The outer disc receives little illumination from the corona and produces only weak reflection and reprocessing features. This scenario explains qualitatively many of the spectral and timing properties of BHBs in the hard state, such as the correlation between X-ray spectral slope and

reflection amplitude (Zdziarski et al., 1999) or Quasi-Periodic Oscillations (QPO) frequencies simply by assuming that the disc inner radius changes for instance with luminosity (Done et al., 2007, see) The location of the disc truncation radius could be determined by a disc evaporation/condensation equilibrium (Meyer et al., 2000; Qiao and Liu, 2012). Figure 1.2 shows a sketch of the possible evolution of the geometry of the accretion flow during an outburst.

Observationally, however, due to the weak disc features the actual transition radius is very difficult to measure accurately. The most recent estimates suggest that in the bright hard state, the inner disc is actually at a few gravitational radii at most (Miller et al., 2015; Parker et al., 2015; Fabian et al., 2015). These results question whether the disc is actually truncated at all. But there is evidence that the disc recedes at low luminosity and the truncation radius could be located much farther out (see Plant et al., 2015).

At least at high luminosities, the hot flow of the truncated disc model cannot be a standard advection-dominated accretion flow (ADAF; Narayan et al. 1997). Indeed, ADAF theory does not predict hot flows that are as bright and as optically thick as observed ($\tau_{\rm T} > 1$) in the bright hard state. The large Thomson depth implies a large density which causes too much cooling for a hot solution to exist at $\tau_{\rm T} > 1$. A possible fix to the model was proposed by Oda et al. (2010, 2012). It consists in assuming the presence of strong magnetic fields in the hot flow. The magnetic field is strong enough to support the hot flow with magnetic pressure rather than the usual thermal pressure. This increases the scale height of the flow and decrease its density, allowing for solutions with larger $\tau_{\rm T}$. In this context, the Thomson depth, electron temperature and coronal luminosity observed in a typical hard state of Cyg X–1 require the magnetic pressure to be a few times larger than thermal pressure (Malzac and Belmont, 2009).

1.4.2 Non-thermal particles

In the soft state there are indications (at least in the prototypical source Cyg X–1) that the hard X-ray emission extends as a power law at least up to a few MeV (McConnell et al., 2002). The absence of cut-off below 1 MeV indicates that the Comptonizing electron distribution of the soft state corona cannot be purely thermal. Producing such gamma-ray emission through inverse Compton requires a power-law like distribution of electrons extending at least up to energies of order of 10-100 times the electron rest mass energy. In the hard state, an excess with respect to a pure Comptonisation model is detected in all bright sources (e.g. Joinet et al., 2007; Droulans et al.,

2010; Jourdain et al., 2012a) which is also interpreted as the signature of a population of non-thermal electrons in the corona.

These findings triggered the development of hybrid thermal/non-thermal Comptonisation models. In these models the Comptonizing electrons have a similar energy distribution in all spectral state i.e. a Maxwellian with the addition of a high energy power-law tail (Poutanen and Coppi, 1998; Coppi, 1999). These models have been extremely successful at fitting the broad band high energy spectra of BHBs. Figure 1.3 shows examples of INTEGRAL spectra fit with an hybrid model. The transition from mostly thermal (in hard state) to mostly non-thermal (in soft state) emitting electrons is understood in terms of the radiation cooling. As a source evolves towards the soft state the corona intercepts a much larger flux of soft photons from the disc. In this more intense soft radiation field the Compton emission of the hot electrons of the plasma is stronger. They radiate their energy faster. This makes the electron temperature significantly lower in softer states. As a consequence, the Compton emissivity of the thermal particles is strongly reduced in the soft state and the emission becomes dominated by the higher energy non-thermal particles. In addition the Thomson depth of thermal electrons is found to be smaller in soft state, possibly because most of the material in the corona has condensed into the disc or is ejected during state transition. This further decreases the luminosity of the Maxwellian component of the plasma, making it barely detectable in soft state. Attempts to model the spectral evolution during spectral state transitions have confirmed that the huge change in the flux of soft cooling photon from the disc illuminating the corona drives the spectral changes of the corona (Del Santo et al., 2008).

The most recent version of the model also includes the radiative effects of magnetic field on the lepton energy distribution (Belmont et al., 2008; Vurm and Poutanen, 2009). Internally generated synchrotron photons (typically in the optical/UV range) constitute a source of seed photons for the Comptonisation process. In addition, the process of Synchrotron self-absorption provides an efficient coupling between leptons which can quickly exchange energy by rapid emission and absorption of synchrotron photons leading to very fast thermalisation of the lepton distribution on time-scales comparable to the light crossing time. In fact, it is not necessary to assume the presence of thermal Comptonizing electrons in the first place. The heating mechanism could be purely non-thermal e.g. accelerating all electrons into a power-law energy distribution. The thermalising effects of the so-called synchrotron boiler (in addition to Coulomb collisions) naturally leads to

an hybrid thermal/non-thermal particle energy (Malzac and Belmont, 2009; Poutanen and Vurm, 2009).

One important effect of the presence of non-thermal electrons in the corona in presence of magnetic field is the production of a strong synchrotron radiation component. The spectral break associated to the transition from optically thick to optically thin synchrotron emission is expected to be located in the optical/IR range. Thermal electrons also produce synchrotron radiation but at a much lower level. Wardziński and Zdziarski (2001) have shown that the addition of a small fraction of non-thermal electrons in the corona (carrying a fraction < 10 % of the total internal energy of the distribution) can increase the optical synchrotron flux by several orders of magnitude. In the framework of the truncated accretion flow model, the hybrid thermal non-thermal distribution of electrons may dominate the optical and IR flux (in hard state) through synchrotron emission, while at the same time explain the hard X-ray through Comptonisation (Veledina et al., 2013a).

1.4.3 X-ray timing

X-ray binaries harbour a strong rapid X-ray variability which presents a very complex and richly documented phenomenology (see Chapter 4 by T. Belloni these proceedings). On the other hand, observations show that most of the X-ray variability occurs on time-scales ranging from 0.1 to 10 s. Strong variability is also observed on longer time-scales. In persistent sources, it was possible to construct long term X-ray fourier power density spectra (PDS) showing a nearly $1/f$ noise extending up to time scales of years (Gilfanov, 2010). In comparison there is virtually no variability on time-scales shorter than 0.01 s. The main problem that any model must overcome is a time-scale problem. Indeed, most of the high energy photons (and variability) must originate deep in the potential from a region of size $R < 100 R_{\rm G} \sim 1500\,{\rm km}$. The times scales in this X-ray emitting region are controlled by dynamical time-scales of the accretion flow such as the Keplerian time-scale

$$t_{\rm K} = 0.3 \left(\frac{M}{10 M_\odot}\right) \left(\frac{R}{50 R_{\rm G}}\right) \qquad {\rm s}, \tag{1.45}$$

or the viscous time-scale (comparable to the accretion time-scale)

$$t_{\rm vis} = \left(\frac{H}{R}\right)^{-2} \frac{t_{\rm K}}{2\pi\alpha}, \tag{1.46}$$

where α is the usual viscosity parameter $\alpha \sim 0.1$ (see Section 1.2.3). In

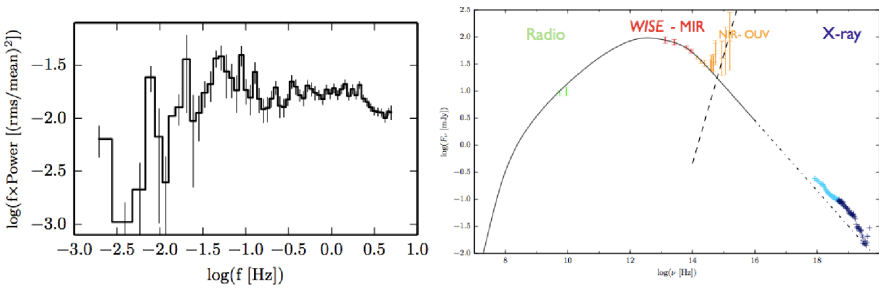

Figure 1.4 Left: the observed X-ray PSD of GX 339–4 during the observations presented in G11. Right: the SED measured by G11 compared to a simulated jet SED obtained assuming that the jet Lorentz factor fluctuations have exactly the PSD as the X-ray flux (Drappeau et al., 2015).

the case of a thin gas pressure dominated accretion disc: $H/R \sim 10^{-2}$ and $t_{\rm vis} \sim 10^4 t_{\rm K} \sim 10^3$ s, while in the case of a hot flow: $H/R \sim 0.3$ an $t_{\rm vis} \sim 10\, t_{\rm K} \sim 1-10$ s. This means that high Fourier frequencies can easily be produced in this region. But the longest observed times scales are too long to be produced in the region of main energy release. They must be generated in the outer parts of the accretion flow.

A possibility could be that fluctuations are generated at large distance and propagate inward. For instance, Lyubarskii (1997) postulates fluctuations in viscosity on local inflow time-scale (itself viscous) over a wide range of distances R from the BH and computes the resulting fluctuations of the mass accretion rate at the inner disc radius. For fluctuation amplitudes that are independent of r, this gives a power spectrum $p(f) \propto 1/f$ i.e. slow variations of large amplitude. In this model the amplitude of the fluctuations generated at a given radius is modulated by the longer fluctuations propagating from the outer region of the disc. For this reason a linear correlation is expected between the the average flux measured within a given time interval and the root-means-squared (RMS) amplitude of the variability during the same time-interval. Such RMS-flux correlations are ubiquitous among accreting BH sources and difficult to produce by any other model (see discussion in Uttley et al. (2005).. Another intriguing feature of the rapid variability of BH binaries is the existence of Fourier frequency dependent delays between X-ray energy bands (the hard photons lagging behind the softer photons). Kotov et al. (2001) improved upon Lyubarskii's model and showed that assuming a harder spectrum close to the BH produces a logarithmic dependence of time-lags on energy, as observed.

The shape and amplitude of the power spectrum changes drastically with spectral state (again, see Chapter 4 by T. Belloni in these proceedings). In

the soft state the RMS amplitude of X-ray variability is at most a few percent, while in the hard state it can reach 30 %. In the hard state the PDS shows band-limited noise. An example of observed X-ray PDS in the hard state is displayed in Figure 1.4. It can be approximatively represented as flat, up to a break frequency $\nu_b \sim 0.01\,\mathrm{Hz}$ at which the slope changes. Above ν_b, the power decreases approximatively as $1/f$ up to a second break at a frequency $\nu_h \sim$ a few Hz. Above ν_h, the PDS decreases now like f^{-2} (or steeper). The observed band limited noise PDS are usually well described in terms of the sum of 4-5 broad Lorentzians (e.g. Nowak 2000; van der Klis 2006). In the truncated disc scenario the band limited noise variability constitutes the variability that is generated due to propagating fluctuations in the hot flow. ν_b is naturally associated as the viscous frequency at the disc inner radius and ν_h is the viscous time-scale at the inner radius of the hot flow which may differ from the ISCO (Done et al., 2007; Ingram and Done, 2011; Ingram et al., 2015).

In addition, a low frequency QPO (LFQPO) is often observed at some intermediate frequency between ν_b and ν_l. This LFQPO is widely believed to be caused by Lense-Thirring (LT) precession of the hot flow (Ingram, Done & Fragile 2009). LT precession is a frame dragging effect associated to the misalignment of the angular momentum of an orbiting particle and the BH spin, leading to precession of the orbit. Numerical simulations have shown that in the case of a hot geometrically thick accretion flow, this effect can lead to global precession of the hot flow (Fragile et al., 2007). The hot flow precesses like a solid body, and the precession frequency is given by a weighted average of the LT precession frequency between inner and outer radii of the flow. Due to much longer viscous scales, the outer thin disc is not expected to be affected by global LT precession. The emission of the precessing hot flow is then naturally modulated due a mixture of relativistic Doppler beaming, light bending and Compton anisotropy. This model predicts the right range of observed LFQPO frequencies. The amplitude of the LFQPO depends on the details of the geometry and inclination of the viewing angle. The RMS is usually larger at high inclinations and can reach 10 % (see also Ingram et al. 2015 for predictions of modulation of the polarization of observed X-ray radiation).

In the truncated disc model the evolution of the disc inner radius drives both the evolution of the photon spectrum and the timing features. As the disc inner radius decreases, ν_b and the LFQPO frequencies are observed to move up, as expected in the model. At the same time, varying the truncation radius change the number of seed soft photons seen by the hot flow and the X-ray spectrum softens as the hot flow becomes gradually more efficiently

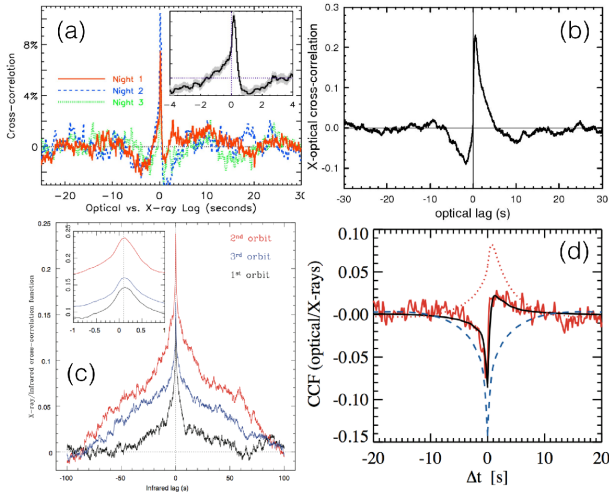

Figure 1.5 Various observed OIR vs X-ray CCFs. Panel (a),(b) and (d) show observed Optical vs X-ray CCFs of GX 339–4 (Gandhi et al., 2008), XTE J1118+480 Kanbach et al. (2001) and Swift J1753-0127 (Veledina et al., 2011) respectively. The CCF of Swift J1753-0127 is modelled with the reprocessing plus hot flow synchrotron model. Panel (c) displays the IR / X-ray CCF observed in GX 339–4 by Casella et al. (2010). ©AAS. Reproduced with permission.

cooled. Such softening of the spectrum is also observed (see e.g. Done et al., 2007).

1.4.4 Optical timing

Besides fast X-ray variability, several accreting BH sources show a strong variability in optical presenting comparable amplitude and PDS (for e.g. see Gandhi, 2009; Gandhi et al., 2010).

Reprocessing model

Part of this variability could be associated to the reprocessing of the X-ray illumination in the outer disc and at the surface of the companion star. If so, the optical reprocessed flux $O(t)$ is expected to respond linearly to the X-ray flux $X(t)$:

$$O(t) = \int_{-\infty}^{t} X(t')r(t-t')dt' \tag{1.47}$$

The response function r can be calculated for given geometry. Such calculations are presented in O'Brien et al. (2002). The reprocessing model predicts

that the optical should be correlated with the X-ray flux and lagging behind the X-ray light curve by a few seconds (light travel time). Moreover the optical is expected to vary on longer time-scales than the X-rays, because the sub-second time-scale variability is strongly damped. Reprocessing is a mechanism that is difficult to avoid and yet these predictions are not always verified.

Fast optical variability from the accretion flow

In several sources the optical fluctuations are observed on comparable or even faster time-scales than the X-rays. The cross-correlation function (CCF) of the X-ay and optical light curves show complex features involving also some level of anti-correlation (see Figure 1.5). The optical time lags can be as short as 100 ms. This suggests an additional variability mechanism in optical. Such a mechanism could be the variable contribution of synchrotron emission by non-thermal coronal particles (Veledina et al., 2011; Poutanen and Veledina, 2014). This emission could be almost as fast as the X-ray fluctuations. In the hybrid thermal-non-thermal hot flow model, moderate fluctuations of the mass accretion rate $\dot{m}$ lead to a simultaneous increase of the plasma Thomson depth and radiation power. Numerical simulations have shown this involves an anti-correlation between X-ray and optical fluxes, which is observed in several sources. Veledina and Poutanen (2015) show that the X-ray and optical variability properties of the source Swift J1753-0127 (shown in Figure 1.5) are well reproduced by a simple model assuming that the optical variability is a mixture of X-ray reprocessing plus a component that is exactly anti-correlated to the X-rays (as expected in the hot flow synchrotron model).

LF QPOs are observed in several hard state sources in the optical band with RMS amplitude ranging from 3 to 30 %. The optical QPOs are sometimes associated to the X-ray LF QPO but not always. These QPOs could originate from the same LT precession mechanisms leading to the formation of the X-ray QPOs. The dominant contribution to the optical synchrotron flux comes from partially self-absorbed synchrotron. The effective synchrotron self-absorption depth depends on viewing angle. Therefore the specific synchrotron intensity produced by the hot flow is modulated by precession

$$I_s \propto 1 - \exp\left[-\tau/\cos\theta(t)\right] \tag{1.48}$$

Depending on the geometric parameters this can lead to QPO amplitudes comparable to those observed (see Veledina et al., 2013b). In principle it

is also possible to predict the phase lags between the X-ray and optical QPOs. Assuming a simple prescription for the angular dependence of the hot flow Comptonized radiation, (Veledina et al., 2013b) predict that the X-ray and optical QPO should be either in phase or in opposition (phase 0 or π). Veledina et al. (2015) show that in Swift J1753.5-0127 the optical and X-ray QPOs are in phase, as predicted by the model. In this source at least the X-ray/optical CCF, the optical and X-ray PDS, their phase lags and coherence spectra are well accounted for by the synchrotron emitting hot flow model.

Another possible origin for the optical LFQPO could be disc reprocessing. Indeed the varying disc illumination caused by the LT precession of the hot flow naturally leads to the modulation of the reprocessed radiation (Veledina & Poutanen 2015). In this case, a QPO is expected only if the hot flow precession period is longer than light crossing time of the disc which is itself a function of the orbital separation of the binary system

$$\nu_{QPOmax} \simeq \frac{c}{R_{disc}} \simeq \frac{2}{3}\left(\frac{P_{\rm orb}}{1{\rm hr}}\right)^{-2/3}\left(\frac{M}{10M_{\odot}}\right)^{-1} \quad {\rm Hz}. \tag{1.49}$$

The amplitude of the QPO, its pulse profile and the expected optical vs X-ray QPO phase lags are expected to depend on the QPO frequency. So far none of the observed optical QPOs matches these properties and are more likely to be caused by synchrotron.

1.4.5 Caveats

In the previous section, the current 'standard' model for the emission of accretion flows around BHs was described. It involves a truncated disc with variable inner radius, a hot inner flow harbouring non-thermal electrons, fluctuations of the mass accretion rate propagating radially inward, and precession of the hot accretion flow. This complex model produces the main features of the emission. In particular the observed simultaneous evolution of the SEDs and X-ray PDS can be understood as driven by changes in the inner disc radius. The observed optical variability and and the correlations between X-ray and optical bands are qualitatively understood. There are however a few issues with this model that should be mentioned. First, the detailed comparison of the hybrid magnetised model with observations has brought interesting constraints on the magnetic field. In the hard state in particular, the conclusion is that either the magnetic field is strongly sub-equipartition (which would be in contradiction with theoretical models

involving a magnetically dominated accretion flow, or accretion disc corona atop the disc), or, the MeV excess is produced in a region that is spatially distinct from that producing the bulk of the hard X-ray radiation (Del Santo et al., 2013).

In the latter case, the accretion flow could for instance, be constituted of a truncated accretion disc surrounding a central magnetically dominated hot accretion flow, responsible for the thermal Comptonisation component, while active coronal regions above and below the outer disc may produce the mostly non-thermal Compton emission (i.e. the hard state MeV excess, Malzac 2012). In the soft state the disc inner radius moves inwards until it reaches the ISCO and the hard X-ray emission becomes gradually dominated by the non-thermal corona. But if the thermal and non-thermal particles are not in the same location, the observed correlations between the X-ray variability and optical synchrotron variability cannot be explained by simultaneous changes in Thomson depth and luminosity. A different interpretation would be required. Another interesting possibility is suggested by INTEGRAL measurements showing that the hard state MeV tail of Cyg X–1 is strongly polarised (at a level of 70 $\pm$30 %), while the thermal Comptonisation emission at lower energy is not (Laurent et al., 2011; Jourdain et al., 2012b)

The only plausible mechanisms for the very high level of polarisation seems to be synchrotron emission in a highly coherent magnetic field. A natural explanation would be that the MeV excess is in fact a contribution from the jet (Romero et al., 2014). Conventional jet models can produce such MeV component but require some fine tuning and quite extreme acceleration parameters (see Zdziarski et al., 2014). If the non-thermal MeV excess is caused by jet synchrotron emission this strongly reduces the possible number of non-thermal electrons in the corona. If so, the coronal optical synchrotron component would be drastically reduced and again, the fast optical variability becomes difficult to explain. As will be shown in the Section 1.5, a possible solution to these problems is to consider the contribution of the jets to the optical and IR emission.

1.5 Model for the jets

In this section we will focus on the emission of BHB jets. The contribution of jets to the X-ray emission of BHBs is a controverted issue but there is evidence that in the most documented sources the jet X-ray emission is weak compared to the emission from the hot flow/corona (see discussion in Malzac 2015 and reference therein). Therefore in this section we will

adopt the conventional view that the X-rays are dominated by the accretion flow. Instead, we will focus on the contribution of jets to the observed fast variability in IR and optical bands (hereafter OIR). Indeed, in OIR, the combination of a reprocessed and a hot flow synchrotron component that is anti-correlated to the X-ray reproduces remarkably the shape of the optical/X-ray CCFs of sources like Swift J1753.5-0127 which show a strong opt/X-ray anti-correlation and a very weak reprocessing peak in their CCFs. However several sources such as GX 339–4 or XTE J1118+480 have an optical X-ray CCF that is very difficult to model because the main peak of the correlation is too narrow to be due to reprocessing and the lag is too small (see Figure 1.5 for a comparison). This suggests some ingredient is missing in the model. Moreover, timing observations of GX 339–4 in IR also show similarly complicated CCFs with sometimes very sharp IR response lagging behind by approximatively 100 ms. Even if the hot flow contains non-thermal electron their synchrotron emission is unlikely to be strong at IR wavelength. The IR variability features have been naturally ascribed to the jets, which are indeed expected to produce IR synchrotron radiation. The 100 ms lag was associated to the travel time for a fluctuation to travel from the disc to jet IR emitting region (C10 Casella et al., 2010). In the following, it will be shown that in fact, the jet could be responsible for most of the observed OIR variability. The interesting consequence is that the observed OIR/X-ray correlation may tell us something about the dynamics of accretion and ejection processes. Such jet models for the OIR variability were initially developed in the early 2000 in the context of the multi-wavelength observations of a very exciting BHB which had recently been discovered: XTE J1118+480 (Remillard et al., 2000). Its relatively close distance ($\simeq$ 1.8 kpc and the exceptionally low interstellar extinction towards the source (Garcia et al., 2000) allowed a multi-wavelength monitoring of the source during its outburst (C03 and reference therein). During the whole outburst duration, the X-ray properties of the source, as well as the presence of strong radio emission, were typical of BH binaries in the hard state. In the radio to optical bands, a strong non-thermal component was associated with synchrotron emission from a powerful jet or outflow (Fender et al., 2001). Interestingly, fast optical and UV photometry allowed by the weak extinction, revealed a rapid optical/UV flickering presenting complex correlations with the X-ray variability (Kanbach et al. 2001; Hynes et al. 2003, hereafter K01 and H03 respectively). This correlated variability cannot be caused by reprocessing of the X-rays in the external parts of the disc. Indeed, the optical flickering occurs on average on shorter time-scales than the X-rays (K01, see Figure 1.6a), and reprocessing models fail to fit the complicated shape of the

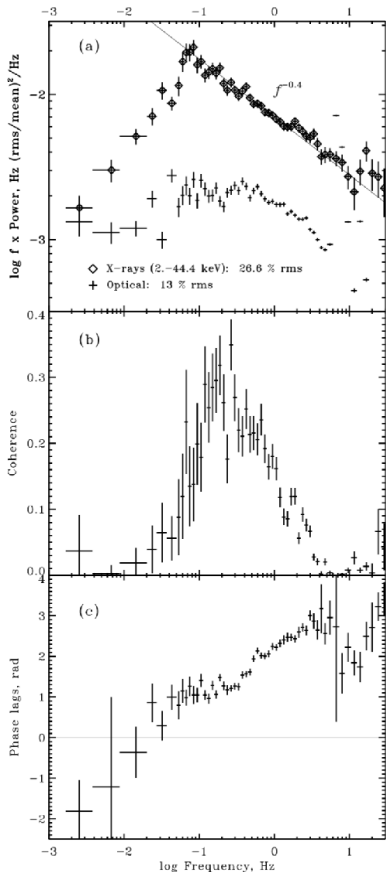

Figure 1.6 The optical/X-ray correlations of XTE J1118+480 in the Fourier domain. a) X-ray and optical power spectra. The counting noise was subtracted (see Section 3.1). b) X-ray/optical coherence. c) phase-lags as function of Fourier frequency. A positive lag implies that the optical is delayed with respect to the X-rays (Malzac et al., 2003). Reproduced with permission ©ESO.

X-ray/optical cross correlation function (H03, see Figure 1.5b). Spectrally, the jet emission seems to extend at least up to the optical band (McClintock et al. (2001), hereafter C03), although the external parts of the disc may provide an important contribution to the observed flux at such wavelengths. The jet activity is thus the most likely explanation for the rapid observed optical flickering. For this reason, the properties of the optical/X-ray correlation in XTE J1118+480 might be of primary importance for the understanding of the jet-corona coupling and the ejection process.

The observations are very challenging for any accretion model. The most

puzzling pieces of evidence are the following: (a) the optical/X-ray CCF shows the optical band lagging the X-ray by 0.5 s, but with a dip 2-5 seconds in advance of the X-rays (K01); (b) the correlation between X-ray and optical light curves appears to have time-scale invariant properties: the X-ray/optical CCF maintains a similar, but rescaled, shape on time-scales ranging at least from 0.1 s to few tens of seconds (Malzac et al., 2003, hereafter M03); (c) the correlation does not appear to be triggered by a single type of event (dip or flare) in the light curves; instead, as was shown by M03, optical and X-ray fluctuations of very different shapes, amplitudes and time-scales are correlated in a similar way, such that the optical light curve is related to the time derivative of the X-ray one. Indeed, in the range of time-scales where the coherence is maximum, the optical/X-ray phase lag are close to $\pi/2$ (see Figure 1.6). This indicates the two light curves are related trough a differential relation. Namely, if the optical variability is representative of fluctuations in the jet power output $P_{\rm j}$, the data suggest that the jet power scales roughly like $P_{\rm j} \propto -\frac{dP_{\rm x}}{dt}$, where $P_{\rm x}$ is the X-ray power.

1.5.1 The energy reservoir model

Malzac et al. (2004, hereafter MMF04) have shown that the complex X-ray/optical correlations could be understood in terms of an energy reservoir model. In this picture, it is assumed that large amounts of accretion power are stored in the accretion flow before being channelled either into the jet (responsible for the variable optical emission) or into particle acceleration/ heating in the Comptonizing region responsible for the X-rays. MMF04 have developed a time dependent model which is complicated in operation and behaviour. However, its essence can be understood using a simple analogue: Consider a tall water tank with an input pipe and two output pipes, one of which is much smaller than the other. The larger output pipe has a tap on it. The flow in the input pipe represents the power injected in the reservoir $P_{\rm i}$, that in the small output pipe the X-ray power $P_{\rm x}$ and in the large output pipe the jet power $P_{\rm j}$. If the system is left alone the water level rises until the pressure causes $P_{\rm i} = P_{\rm j} + P_{\rm x}$. Now consider what happens when the tap is opened more, causing $P_{\rm j}$ to rise. The water level and pressure (proportional to E) drop causing $P_{\rm x}$ to reduce. If the tap is then partly closed, the water level rises, $P_{\rm j}$ decreases and $P_{\rm x}$ increases. The rate $P_{\rm x}$ depends upon the past history, or integral of $P_{\rm j}$. Identifying the optical flux as a marker of $P_{\rm j}$ and the X-ray flux as a marker of $P_{\rm x}$ we obtain the basic behaviour seen in XTE J1118+480. In the real situation, MMF04 envisage that the variations in the tap are stochastically controlled by a shot noise process.

There are also stochastically-controlled taps on the input and other output pipes as well. The overall behaviour is therefore complex. The model shows however that the observed complex behaviour of XTE J1118+480 can be explained by a relatively simple basic model involving several energy flows and an energy reservoir. This simple model is largely independent of the physical nature of the energy reservoir. In a real accretion flow, the reservoir could take the form of either electromagnetic energy stored in the X-ray emitting region, or thermal (hot protons) or turbulent motions. The material in the disc could also constitute a reservoir of gravitational or rotational energy behaving as described above. In a stationary flow, the extracted power $P_{\rm j} + P_{\rm x}$ would be perfectly balanced by the power injected, which is, in the most general case, given by the difference between the accretion power and the power advected into the hole and/or stored in convective motions: $P_i \simeq \dot{M}c^2 - P_{\rm adv,conv}$. However, observations of strong variability on short time scale clearly indicate that the heating and cooling of the X-ray (and optical) emitting plasma are highly transient phenomena, and the corona is unlikely to be in complete energy balance on short time-scales. MMF04 therefore introduced a time-dependent equation governing the evolution of its total energy E

$$\dot{E} \;=\; P_{\rm i} - P_{\rm j} - P_{\rm x}, \tag{1.50}$$

and we assume that all the three terms on the right hand side are time dependent. The optical variability is produced mainly from synchrotron emission in the inner part of the jet at distances of a few thousands gravitational radii from the hole. We assume that at any time the optical flux O_{pt} (resp. X-ray flux) scales like the jet power $P_{\rm j}$ (plasma heating power $P_{\rm x}$). MMF04 introduced the instantaneous dissipation rates $K_{\rm j}$ and $K_{\rm x}$

$$P_{\rm j}(t) \;=\; K_{\rm j}(t)E(t), \qquad P_{\rm x}(t) \;=\; K_{\rm x}(t)E(t), \tag{1.51}$$

For a specific set of parameters MMF04 generate random independent fluctuations (time series) for $K_{\rm x}$, $K_{\rm j}$ and $P_{\rm i}$, solve the time evolution of the energy reservoir E and then use the solution to derive the the resulting optical and X-ray light curves (see MMF04 for details).

Combining equations (1.50) and (1.51) we obtain the following relation for the total instantaneous jet power

$$P_{\rm j} \;=\; P_{\rm i} - (1 + \frac{\dot{K}_{\rm x}}{K_{\rm x}^2})P_{\rm x} - \dot{P}_{\rm x}/K_{\rm x}. \tag{1.52}$$

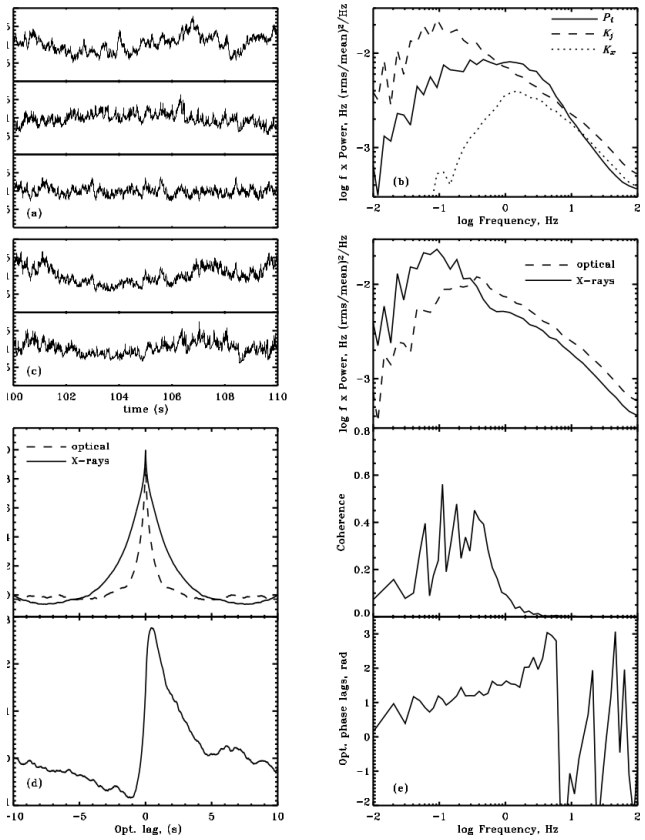

Figure 1.7 Sample input time series (panel a) and power spectra (panel b) of $P_{\rm i}$, $K_{\rm j}$, $K_{\rm x}$, resulting X-ray and optical fluxes light curves (panel c), X-ray/optical autocorrelation and cross-correlation functions (panel d), power spectra, coherence and phase-lags (panel e) (From Malzac et al., 2004).

We can see from this equation that the differential scaling $P_{\rm j} \propto -\dot{P}_{\rm x}$, observed in XTE J1118+480, will be rigorously reproduced provided that: (1) $K_{\rm x}$ is a constant; (2) $P_{\rm i} - P_{\rm x}$ is a constant. It is physically unlikely that those conditions will be exactly verified. In particular, $P_{\rm x}$ is observed to have a large RMS amplitude of variability of about 30 %. However, the observed differential relation holds only roughly and only for fluctuations within a relatively narrow range of time-scales $1 - 10s$. Therefore, the above conditions need only to be fulfilled approximatively and for low frequency fluctuations ($>$ 1s). In practice, the following requirements will be enough to make sure that the low frequency fluctuations of the right hand side of equation 1.52 are dominated by $\dot{P}_{\rm x}$:

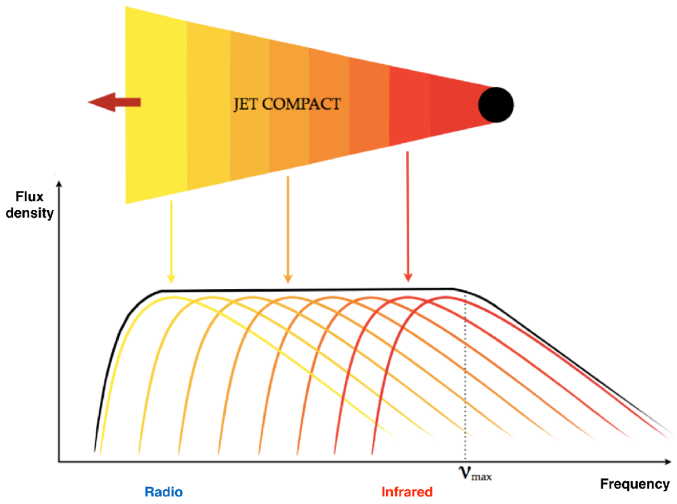

Figure 1.8 The jet SED is made of the contribution of synchrotron emitting regions distributed over the jet length (Fermi LAT Collaboration et al., 2010).

- $P_x \ll P_i$, implying that the jet power, on average, dominates over the X-ray luminosity;
- the amplitude of variability of K_x and P_i in the 1–10 s range is low compared to that of P_j. In other words the 1–10 s fluctuations of the system are mainly driven by the jet activity, implying that the mechanisms for dissipation in the jet and the corona occur on quite different time-scales.

Figure 1.7 shows the results of a simulation matching the main timing properties of XTE J1118+480. In this simulation jet power was set to be 10 times larger than the X-ray power. As can be seen, the resulting PSDs, CCFs, phase-lag and coherence spectra are very similar to those observed in XTE J1118+480.

1.5.2 Internal shock model

The puzzling optical/X-ray correlations of XTE J1118+480, can be understood in terms of a common energy reservoir for both the jet and the Comptonizing electrons. However the model outlined above remains a toy model and more realistic jet physics must be taken into account. In particular we have to explain how jet radiation is produced. The flat SED of compact jets are usually ascribed to self-absorbed synchrotron emission in a conical jet geometry (Blandford and Königl, 1979). The model postulates the

presence of a standing shock located close to the base of the jet (at distances ranging between 10^3 to 10^4 $R_{\rm G}$ from the BH. In this shock electrons are accelerated with a power-law energy distribution extending up to ultra-relativistic energies and then propagate along the jet with the flow while radiating synchrotron radiation. As the electrons travel in this conical geometry their density decreases and the peak of synchrotron emission (which corresponds to the turn-over frequency between optically thin and optically thick synchrotron, see Section 1.3.1) moves toward longer wavelengths. The jet SED is made of the sum of the emitting electrons distributed all along the the jet. The radio emission is produced at large distance while the IR is produced close to the initial acceleration region (see Figure 1.8). A flat spectrum is produced under the assumption of continuous energy replenishment of the adiabatic expansion losses. Adiabatic expansion losses are simply the internal energy losses of the gas (and tangled magnetic field) due to pressure work against the external medium as it expands in the conical geometry. The compensation of these energy losses is crucial for maintaining this specific spectral shape (Kaiser, 2006). Some dissipation mechanism is required to compensate for these losses otherwise the radio emission is strongly suppressed and the jet SED is too inverted.

Internal shocks provide a possible mechanism to compensate for the adiabatic expansion losses by dissipating energy and accelerating particles at large distance from the BH. Internal shocks caused by fluctuations of the outflow velocity are indeed widely believed to power the multi-wavelength emission of jetted sources such as γ-ray bursts (Rees and Meszaros, 1994; Daigne and Mochkovitch, 1998), active galactic nuclei (Rees, 1978; Spada et al., 2001), or microquasars (Kaiser et al., 2000; Jamil et al., 2010). . Internal shocks models usually assume that the jet can be discretised into homogeneous ejectas. Those ejectas are injected at the base of the jet with variable velocities and then propagate along the jet. At some point, the fastest fluctuations start catching up and merging with slower ones. This leads to shocks in which a fraction of the bulk kinetic velocity of the shells is converted into internal energy. Part of the dissipated energy goes into particles acceleration, leading to synchrotron and also, possibly, inverse Compton emission.

The energy dissipation profile of the internal shocks is very sensitive to the shape of the PSD of the velocity fluctuations. Indeed, let us consider a fluctuation of the jet velocity of amplitude Δv occuring on a time-scale Δt. This leads to the formation of a shock at a downstream distance $z_s \propto \Delta t/\Delta v$. In this shock the fraction of the kinetic energy converted into internal energy will be larger for larger Δv. From these simple considerations we see that the

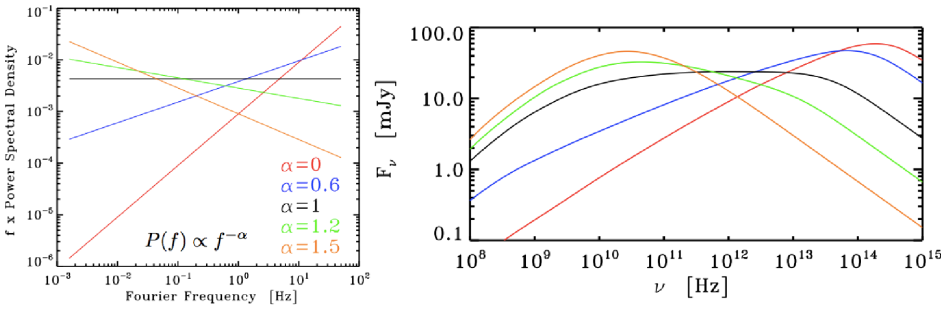

Figure 1.9 Simulation of the internal shock model with a power-law PSD of the Lorentz factor fluctuations ($P(f) \propto f^{-\alpha}$). The top left panel shows the shape of the injected PSDs, for the indicated values of the α index. The right panel shows the jet SED calculated for an inclination angle of 40 degrees and a distance to the source of 2 Kpc. (see Malzac, 2014; Malzac and Drappeau, 2015, for details)

distribution of the velocity fluctuation amplitudes over their time-scales (i.e. the PSD) is going to determine where and in which amount the energy of the internal shocks is deposited. Malzac (2012) used Monte-Carlo simulations to study this dependance and found that independently of the details of the model flat radio-IR SEDs are obtained for a flicker noise PSD of the fluctuations of the jet Lorentz factor. This result is illustrated by Figure 1.9, which compares the SEDs obtained for PSD of the Lorentz factor of the jet with a power-law shape with varying index α: $P(f) \propto f^{-\alpha}$. For larger α the fluctuations of the Lorentz factor have, on average, longer time-scales and therefore more dissipation occurs at larger distances from the BH. One can see from Figure 1.9 that the SED is very sensitive to the value of α, for $\alpha = 1$ (i.e. flicker noise) the dissipation profile scales like z^{-1} and the specific energy profile is flat. In other words, the internal shocks compensate exactly for the adiabatic losses. As result the SED is flat over a wide range of photon frequencies. In fact, this result can also be obtained analytically (Malzac 2013). The case of flicker noise fluctuations of the jet Lorentz factor may therefore be relevant to the observations of compact jets.

An interesting feature of the internal shock model is that it naturally predicts strong variability of the jet emission. Figure 1.10 shows sample light curves and power spectra obtained from the simulation with $\alpha = 1$. The jet behaves like a low-pass filter. As the shells of plasma travel down the jet, colliding and merging with each other, the highest frequency velocity fluctuations are gradually damped and the size of the emitting region increases. The jet is strongly variable in the optical and IR bands originating primarily

from the base of the emitting region and becomes less and less variable at longer frequencies produced at larger distances from the BH.

Note that strong coherent periodic fluctuations of of the jet Lorentz factor may lead to the formation of QPO features in the jet variability. However, in the context of the jet model a much more likely explanation for the observed optical and IR QPOs could be the precession of the jets. Indeed if the X-ray LF QPOs are caused by global LT precession of the hot flow and if the jet is launched from the accretion flow, one may expects the jet to precesses with the flow. The (mostly) optically thin synchrotron radiation observed in IR and optical would then be modulated at the precession frequency due to the modulation of Doppler beaming effects toward the observer (Kalamkar et al., 2016).

The model may be used to understand the observed complex timing correlation between the X-ray and IR bands. For example, C10 measured de CCF of the X-ray and IR light curves and found significant correlation between the two bands with the IR photons lagging behind the X-rays by about 100 ms (see Figure 1.5c). C10 interpreted this time-lag as the propagation time of the ejected shells from the accretion flow to the IR emitting region in the jet. In the framework of the internal shock model this observation suggests that the fluctuations of the jet Lorentz factor are related to the X-ray variability of the source. Malzac , 2014 shows that the internal shock model predict very similar IR vs X-ray CCF and lags. provided that the fluctuation of the bulk jet Lorentz factor are inversely proportional to the X-ray flux.

1.5.3 Are the jet Lorentz factor fluctuations related to the X-ray variability ?

In fact, if the jet is launched from the accretion disc, the variability of the jet Lorentz factor must be related to that of the accretion disc. And we know, both from theory (see e.g. Lyubarskii, 1997) and from observations(see e.g. Gilfanov and Arefiev, 2005) that accretion discs tend to generate flicker noise variability. Therefore flicker noise fluctuations of the jet Lorentz factor are not unexpected. In X-ray binaries the variability of the accretion flow is best traced directly by the X-ray light curves. The left panel of Figure 1.4 shows an actual X-ray PDS oserve in GX 339–4 in the hard state, which differs significantly from flicker noise both at high and low frequencies. This variability could be a good proxy for the assumed fluctuations of the jet. The right panel of Figure 1.4 shows the resulting time averaged SED obtained if one assume that the Lorentz factor fluctuations have a PSD that is exactly

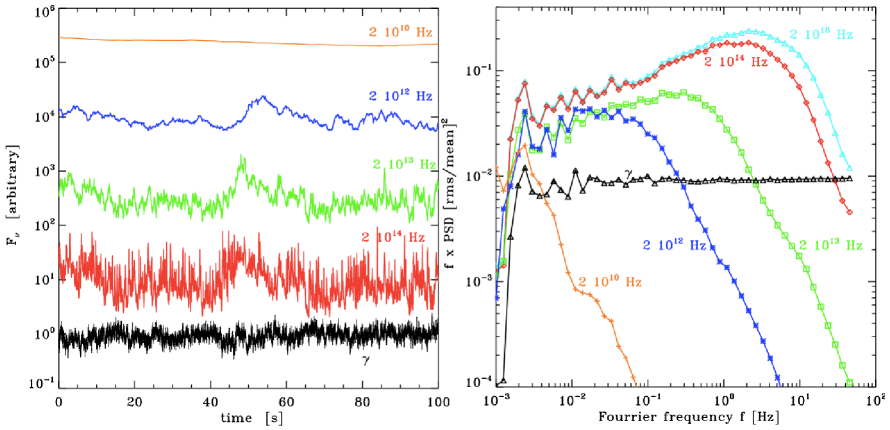

Figure 1.10 Synthetic light curves (left, rescaled) and power spectra at various indicated frequencies resulting from the simulation with $\alpha = 0$. The injected fluctuations of the Lorentz factor are also shown. (Malzac, 2014).

that observed in X-rays. This synthetic SED is compared to multi wavelength observation that are nearly simultaneous with the X-ray timing data (see Drappeau et al., 2015, for details). The model appears to reproduce pretty well the radio to IR data. This agreement is striking because the shape of the SED depends almost uniquely on the assumed shape of the PSD of the fluctuations. Although the model has a number of free parameters (jet power, inclination angle, time-averaged jet Lorentz factor...) that could be tuned to fit the data, those parameters only affect the flux normalisation or shift in the photon frequency direction, but they have very little effects on the overall shape of the SED.

The four mid-IR flux measurements at 1.36×10^{13}, 2.50×10^{13}, 6.52×10^{13} and 8.82×10^{13} Hz that are shown on Figure 1.4 were obtained with the Wide field Infrared Survey Explorer (WISE Wright et al., 2010) they represent an average over 13 epochs, sampled at multiples of the satellite orbital period of 95 minutes and with a shortest sampling interval of 11 s, when WISE caught the source on two consecutive scans. These data have revealed a strong variability of the mid-IR emission (see G11). The light curves of these observations are shown in Figure 1.11 (left panel) and compared to light curves obtained from the same simulation that gives a good fit to the observed radio-IR SED (right panel). The model appears to predict a variability of similar amplitude to that observed by WISE.

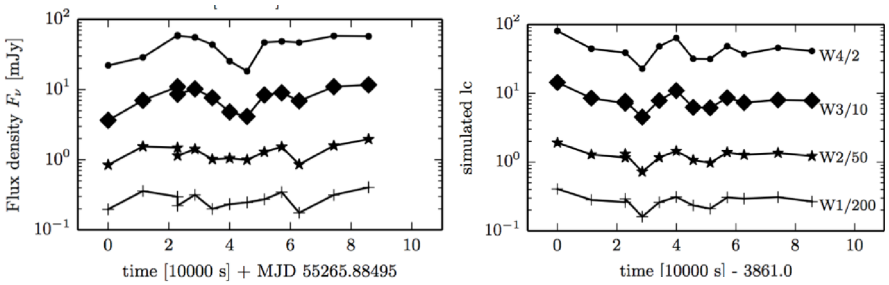

Figure 1.11 Left: the observed mid-IR variability as observed by WISE in 4 bands. Right: sample synthetic light curves obtained from the same simulation shown in Figure 1.4. (Malzac and Drappeau, 2015).

1.6 Conclusion

Compact objects can release huge amounts of energy on very short timescales through extraction of their own rotational energy, dissipation of their powerfull magnetic fields, of the gravitational energy of accreted material which can be also gravitationally compressed to the point of thermonuclear fusion. A fraction of this energy is converted into radiation that is emitted non-thermally through synchrotron, curvature radiation inverse Compton, Bremsstrahlung. Based on the properties of these radiation processes and the energy dissipation mechanisms, time-dependent emission models are developed which, through comparison to data, allow to constrain the physical conditions in the emitting regions. Such comparisons may also may shed new lights on the physics of compact objects requiring in turn to revise the models. In the the particular case of accreting BHBs, the truncated disc model including a hot inner flow with non-thermal electrons, fluctuations of the mass accretion rate propagating radially inward, and precession of the hot accretion flow produces the main features of the multi-wavelength spectra and variability. In particular in some sources, the observed optical variability and and the correlations between X-ray and optical bands are qualitatively understood. However in some other sources a strong contribution of the jet to the IR and perhaps even optical variability seem to be required. Fast jet synchrotron variability may results from the disc variability through a tight coupling between jet and accretion flow on short timescales, possibly through a common energy reservoir. The IR jet radiation is likely to produced through synchrotron emission of particules accelerated in colliding shells of gas (internal shocks). This internal shock model naturally predicts the formation of the observed SEDs of compact jets and also predict a strong, wavelength dependent, variability that resembles the observed one.

The model also suggests a strong connection between the observable properties of the jet in the radio to IR bands, and the variability of the accretion flow as observed in X-rays. If the model is correct, this offers a unique possibility to probe the dynamics of the coupled accretion and ejection processes leading to the formation of compact jets. Future multifrequency HTRA observations combined with further modelling may reveal this fast dynamic coupling.

1.7 Acknowledgments

I am extremely grateful to the organisers of this Winter School, T. Shahbaz, J. Casares and T. Muñoz Darias, for inviting me at the Instituto de Astrofísica de Canarias and for the opportunity to deliver these lectures. I also want to thank my long-time collaborator Renaud Belmont for his inputs, in particular the material he provided for the section on radiation processes. The preparation of this manuscript was supported in part by the ANR CHAOS project ANR-12-BS05-0009 (http://www.chaos-project.fr).

References

Balbus, S. A., and Hawley, J. F. 1991. A powerful local shear instability in weakly magnetized disks. I - Linear analysis. II - Nonlinear evolution. ApJ, **376**(July), 214–233.

Balbus, S. A., and Hawley, J. F. 1998. Instability, turbulence, and enhanced transport in accretion disks. *Reviews of Modern Physics*, **70**(Jan.), 1–53.

Belmont, R., Malzac, J., and Marcowith, A. 2008. Simulating radiation and kinetic processes in relativistic plasmas. A&A, **491**(Nov.), 617–631.

Beloborodov, A. M. 1999. Accretion Disk Models. Page 295 of: Poutanen, J., and Svensson, R. (eds), *High Energy Processes in Accreting Black Holes*. Astronomical Society of the Pacific Conference Series, vol. 161.

Blandford, R. D., and Begelman, M. C. 1999. On the fate of gas accreting at a low rate on to a black hole. MNRAS, **303**(Feb.), L1–L5.

Blandford, R. D., and Königl, A. 1979. Relativistic jets as compact radio sources. ApJ, **232**(Aug.), 34–48.

Blandford, R. D., and Payne, D. G. 1982. Hydromagnetic flows from accretion discs and the production of radio jets. MNRAS, **199**(June), 883–903.

Blandford, R. D., and Znajek, R. L. 1977. Electromagnetic extraction of energy from Kerr black holes. MNRAS, **179**(May), 433–456.

Bondi, H. 1952. On spherically symmetrical accretion. MNRAS, **112**, 195.

Bondi, H., and Hoyle, F. 1944. On the mechanism of accretion by stars. MNRAS, **104**, 273.

Cabanac, C., Fender, R. P., Dunn, R. J. H., and Körding, E. G. 2009. On the variation of black hole accretion disc radii as a function of state and accretion rate. MNRAS, **396**(July), 1415–1440.

Casella, P., Maccarone, T. J., O'Brien, K., Fender, R. P., Russell, D. M., van der Klis, M., Pe'Er, A., Maitra, D., Altamirano, D., Belloni, T., Kanbach, G., Klein-Wolt, M., Mason, E., Soleri, P., Stefanescu, A., Wiersema, K., and Wijnands, R. 2010. Fast infrared variability from a relativistic jet in GX 339-4. MNRAS, **404**(May), L21–L25.

Chaty, S., Haswell, C. A., Malzac, J., Hynes, R. I., Shrader, C. R., and Cui, W. 2003. Multiwavelength observations revealing the evolution of the outburst of the black hole XTE J1118+480. MNRAS, **346**(Dec.), 689–703.

Christodoulou, D. 1970. Reversible and Irreversible Transformations in Black-Hole Physics. *Physical Review Letters*, **25**(Nov.), 1596–1597.

Coppi, P. S. 1999. The Physics of Hybrid Thermal/Non-Thermal Plasmas. Page 375 of: Poutanen, J., and Svensson, R. (eds), *High Energy Processes in Accreting Black Holes*. Astronomical Society of the Pacific Conference Series, vol. 161.

Corbel, S., and Fender, R. P. 2002. Near-Infrared Synchrotron Emission from the Compact Jet of GX 339-4. ApJ, **573**(July), L35–L39.

Daigne, F., and Mochkovitch, R. 1998. Gamma-ray bursts from internal shocks in a relativistic wind: temporal and spectral properties. MNRAS, **296**(May), 275–286.

Davidson, K., and Ostriker, J. P. 1973. Neutron-Star Accretion in a Stellar Wind: Model for a Pulsed X-Ray Source. ApJ, **179**(Jan.), 585–598.

Davis, S. W., Blaes, O. M., Hubeny, I., and Turner, N. J. 2005. Relativistic Accretion Disk Models of High-State Black Hole X-Ray Binary Spectra. ApJ, **621**(Mar.), 372–387.

Davis, S. W., Done, C., and Blaes, O. M. 2006. Testing Accretion Disk Theory in Black Hole X-Ray Binaries. ApJ, **647**(Aug.), 525–538.

Del Santo, M., Malzac, J., Jourdain, E., Belloni, T., and Ubertini, P. 2008. Spectral variability of GX339-4 in a hard-to-soft state transition. MNRAS, **390**(Oct.), 227–234.

Del Santo, M., Malzac, J., Belmont, R., Bouchet, L., and De Cesare, G. 2013. The magnetic field in the X-ray corona of Cygnus X-1. MNRAS, **430**(Mar.), 209–220.

Done, C., Gierliński, M., and Kubota, A. 2007. Modelling the behaviour of accretion flows in X-ray binaries. Everything you always wanted to know about accretion but were afraid to ask. A&A Rev., **15**(Dec.), 1–66.

Drappeau, S., Malzac, J., Belmont, R., Gandhi, P., and Corbel, S. 2015. Internal shocks driven by accretion flow variability in the compact jet of the black hole binary GX 339-4. MNRAS, **447**(Mar.), 3832–3839.

Droulans, R., Belmont, R., Malzac, J., and Jourdain, E. 2010. Variability and Spectral Modeling of the Hard X-ray Emission of GX 339-4 in a Bright Low/Hard State. ApJ, **717**(July), 1022–1036.

Dunn, R. J. H., Fender, R. P., Körding, E. G., Belloni, T., and Merloni, A. 2011. A global study of the behaviour of black hole X-ray binary discs. MNRAS, **411**(Feb.), 337–348.

Esin, A. A., McClintock, J. E., and Narayan, R. 1997. Advection-Dominated Accretion and the Spectral States of Black Hole X-Ray Binaries: Application to Nova Muscae 1991. ApJ, **489**(Nov.), 865–889.

Fabian, A. C., Lohfink, A., Kara, E., Parker, M. L., Vasudevan, R., and Reynolds, C. S. 2015. Properties of AGN coronae in the NuSTAR era. MNRAS, **451**(Aug.), 4375–4383.

Fender, R., and Gallo, E. 2014. An Overview of Jets and Outflows in Stellar Mass Black Holes. Space Sci. Rev., **183**(Sept.), 323–337.

Fender, R. P., Pooley, G. G., Durouchoux, P., Tilanus, R. P. J., and Brocksopp, C. 2000. The very flat radio-millimetre spectrum of Cygnus X-1. MNRAS, **312**(Mar.), 853–858.

Fender, R. P., Hjellming, R. M., Tilanus, R. P. J., Pooley, G. G., Deane, J. R., Ogley, R. N., and Spencer, R. E. 2001. Spectral evidence for a powerful compact jet from XTE J1118+480. MNRAS, **322**(Apr.), L23–L27.

Fermi LAT Collaboration et al. 2009. Modulated High-Energy Gamma-Ray Emission from the Microquasar Cygnus X-3. *Science*, **326**(Dec.), 1512.

Fermi LAT Collaboration et al. 2010. *Jets relativistes des trous noirs accrtants.* Ph.D. thesis, Paris.

Fragile, P. C., Blaes, O. M., Anninos, P., and Salmonson, J. D. 2007. Global General Relativistic Magnetohydrodynamic Simulation of a Tilted Black Hole Accretion Disk. ApJ, **668**(Oct.), 417–429.

Frank, J., King, A., and Raine, D. 1992. *Accretion power in astrophysics.* Cambridge University Press.

Galeev, A. A., Rosner, R., and Vaiana, G. S. 1979. Structured coronae of accretion disks. ApJ, **229**(Apr.), 318–326.

Gandhi, P. 2009. The Flux-Dependent rms Variability of X-Ray Binaries in the Optical. ApJ, **697**(June), L167–L172.

Gandhi, P., Makishima, K., Durant, M., Fabian, A. C., Dhillon, V. S., Marsh, T. R., Miller, J. M., Shahbaz, T., and Spruit, H. C. 2008. Rapid optical and X-ray timing observations of GX 339-4: flux correlations at the onset of a low/hard state. MNRAS, **390**(Oct.), L29–L33.

Gandhi, P., Dhillon, V. S., Durant, M., Fabian, A. C., Kubota, A., Makishima, K., Malzac, J., Marsh, T. R., Miller, J. M., Shahbaz, T., Spruit, H. C., and Casella, P. 2010. Rapid optical and X-ray timing observations of GX339-4: multicomponent optical variability in the low/hard state. MNRAS, **407**(Oct.), 2166–2192.

Gandhi, P., Blain, A. W., Russell, D. M., Casella, P., Malzac, J., Corbel, S., D'Avanzo, P., Lewis, F. W., Markoff, S., Cadolle Bel, M., Goldoni, P., Wachter, S., Khangulyan, D., and Mainzer, A. 2011. A Variable Mid-infrared Synchrotron Break Associated with the Compact Jet in GX 339-4. ApJ, **740**(Oct.), L13.

Garcia, M., Brown, W., Pahre, M., McClintock, J., Callanan, P., and Garnavich, P. 2000. XTE J1118+480. IAU Circ., **7392**(Apr.).

Ghisellini, G., and Svensson, R. 1991. The synchrotron and cyclo-synchrotron absorption cross-section. MNRAS, **252**(Oct.), 313–318.

Gierliński, M., and Done, C. 2004. Black hole accretion discs: reality confronts theory. MNRAS, **347**(Jan.), 885–894.

Gilfanov, M. 2010 (Mar.). X-Ray Emission from Black-Hole Binaries. Page 17 of: Belloni, T. (ed), *Lecture Notes in Physics, Berlin Springer Verlag.* Lecture Notes in Physics, Berlin Springer Verlag, vol. 794.

Gilfanov, M., and Arefiev, V. 2005. X-ray variability, viscous time scale and Lindblad resonances in LMXBs. *ArXiv Astrophysics e-prints*, Jan.

Gilfanov, M. R., and Sunyaev, R. A. 2014. Radiation-dominated boundary layer between an accretion disc and the surface of a neutron star: theory and observations. *Physics Uspekhi*, **57**(Apr.), 377–388.

Haardt, F., and Maraschi, L. 1993. X-ray spectra from two-phase accretion disks. ApJ, **413**(Aug.), 507–517.

Haardt, F., Maraschi, L., and Ghisellini, G. 1994. A model for the X-ray and ultraviolet emission from Seyfert galaxies and galactic black holes. ApJ, **432**(Sept.), L95–L99.

Harding, A. K. 2013. The neutron star zoo. *Frontiers of Physics*, **8**(Dec.), 679–692.

Hynes, R. I., Haswell, C. A., Cui, W., Shrader, C. R., O'Brien, K., Chaty, S., Skillman, D. R., Patterson, J., and Horne, K. 2003. The remarkable rapid X-ray, ultraviolet, optical and infrared variability in the black hole XTE J1118+480. MNRAS, **345**(Oct.), 292–310.

Ingram, A., and Done, C. 2011. A physical model for the continuum variability and quasi-periodic oscillation in accreting black holes. MNRAS, **415**(Aug.), 2323–2335.

Ingram, A., Maccarone, T. J., Poutanen, J., and Krawczynski, H. 2015. Polarization Modulation from Lense-Thirring Precession in X-Ray Binaries. ApJ, **807**(July), 53.

Inogamov, N. A., and Sunyaev, R. A. 1999. Spread of matter over a neutron-star surface during disk accretion. *Astronomy Letters*, **25**(May), 269–293.

Jackson, John David. 1999. *Classical electrodynamics*. New York: J. Wiley & sons.

Jamil, O., Fender, R. P., and Kaiser, C. R. 2010. iShocks: X-ray binary jets with an internal shocks model. MNRAS, **401**(Jan.), 394–404.

Joinet, A., Jourdain, E., Malzac, J., Roques, J. P., Corbel, S., Rodriguez, J., and Kalemci, E. 2007. Hard X-Ray Emission of the Microquasar GX 339-4 in the Low/Hard State. ApJ, **657**(Mar.), 400–408.

Jourdain, E., Roques, J. P., Chauvin, M., and Clark, D. J. 2012a. Separation of Two Contributions to the High Energy Emission of Cygnus X-1: Polarization Measurements with INTEGRAL SPI. ApJ, **761**(Dec.), 27.

Jourdain, E., Roques, J. P., and Malzac, J. 2012b. The Emission of Cygnus X-1: Observations with INTEGRAL SPI from 20 keV to 2 MeV. ApJ, **744**(Jan.), 64.

Kaiser, C. R. 2006. The flat synchrotron spectra of partially self-absorbed jets revisited. MNRAS, **367**(Apr.), 1083–1094.

Kaiser, C. R., Sunyaev, R., and Spruit, H. C. 2000. Internal shock model for microquasars. A&A, **356**(Apr.), 975–988.

Kalamkar, M., Casella, P., Uttley, P., O'Brien, K., Russell, D., Maccarone, T., van der Klis, M., and Vincentelli, F. 2016. Detection of the first infra-red quasi-periodic oscillation in a black hole X-ray binary. MNRAS, **460**(Aug.), 3284–3291.

Kanbach, G., Straubmeier, C., Spruit, H. C., and Belloni, T. 2001. Correlated fast X-ray and optical variability in the black-hole candidate XTE J1118+480. Nature, **414**(Nov.), 180–182.

Kato, S., Fukue, J., and Mineshige, S. 2008. *Black-Hole Accretion Disks — Towards a New Paradigm —*. Kyoto University Press.

Kotov, O., Churazov, E., and Gilfanov, M. 2001. On the X-ray time-lags in the black hole candidates. MNRAS, **327**(Nov.), 799–807.

Lamb, F. K., Pethick, C. J., and Pines, D. 1973. A Model for Compact X-Ray Sources: Accretion by Rotating Magnetic Stars. ApJ, **184**(Aug.), 271–290.

Laurent, P., Rodriguez, J., Wilms, J., Cadolle Bel, M., Pottschmidt, K., and Grinberg, V. 2011. Polarized Gamma-Ray Emission from the Galactic Black Hole Cygnus X-1. *Science*, **332**(Apr.), 438.

Longair, M. S. 1992. *High energy astrophysics. Vol.1: Particles, photons and their detection.* Cambridge University Press.

Longair, M. S. 1994. *High energy astrophysics. Volume 2. Stars, the Galaxy and the interstellar medium.* Cambridge University Press.

Lyubarskii, Y. E. 1997. Flicker noise in accretion discs. MNRAS, **292**(Dec.), 679.

Malyshev, D., Zdziarski, A. A., and Chernyakova, M. 2013. High-energy gamma-ray emission from Cyg X-1 measured by Fermi and its theoretical implications. MNRAS, **434**(Sept.), 2380–2389.

Malzac, J. 2012. On the Nature of the X-Ray Corona of Black Hole Binaries. *International Journal of Modern Physics Conference Series*, **8**, 73–83.

Malzac, J. 2014. The spectral energy distribution of compact jets powered by internal shocks. MNRAS, **443**(Sept.), 299–317.

Malzac, J., and Belmont, R. 2009. The synchrotron boiler and the spectral states of black hole binaries. MNRAS, **392**(Jan.), 570–589.

Malzac, J., and Drappeau, S. 2015 (Dec.). The emission of compact jets powered by internal shocks. Pages 161–165 of: Martins, F., Boissier, S., Buat, V., Cambrésy, L., and Petit, P. (eds), *SF2A-2015: Proceedings of the Annual meeting of the French Society of Astronomy and Astrophysics.*

Malzac, J., Beloborodov, A. M., and Poutanen, J. 2001. X-ray spectra of accretion discs with dynamic coronae. MNRAS, **326**(Sept.), 417–427.

Malzac, J., Belloni, T., Spruit, H. C., and Kanbach, G. 2003. The optical and X-ray flickering of XTE J1118+480. A&A, **407**(Aug.), 335–345.

Malzac, J., Merloni, A., and Fabian, A. C. 2004. Jet-disc coupling through a common energy reservoir in the black hole XTE J1118+480. MNRAS, **351**(June), 253–264.

Marcowith, A., and Malzac, J. 2003. Cyclotron-synchrotron: Harmonic fitting functions in the non-relativistic and trans-relativistic regimes. A&A, **409**(Oct.), 9–19.

McClintock, J. E., Haswell, C. A., Garcia, M. R., Drake, J. J., Hynes, R. I., Marshall, H. L., Muno, M. P., Chaty, S., Garnavich, P. M., Groot, P. J., Lewin, W. H. G., Mauche, C. W., Miller, J. M., Pooley, G. G., Shrader, C. R., and Vrtilek, S. D. 2001. Complete and Simultaneous Spectral Observations of the Black Hole X-Ray Nova XTE J1118+480. ApJ, **555**(July), 477–482.

McConnell, M. L., Zdziarski, A. A., Bennett, K., Bloemen, H., Collmar, W., Hermsen, W., Kuiper, L., Paciesas, W., Phlips, B. F., Poutanen, J., Ryan, J. M., Schönfelder, V., Steinle, H., and Strong, A. W. 2002. The Soft Gamma-Ray Spectral Variability of Cygnus X-1. ApJ, **572**(June), 984–995.

Mereghetti, S., La Palombara, N., Tiengo, A., Pizzolato, F., Esposito, P., Woudt, P. A., Israel, G. L., and Stella, L. 2011. X-Ray and Optical Observations of the Unique Binary System HD 49798/RX J0648.0-4418. ApJ, **737**(Aug.), 51.

Meyer, F., Liu, B. F., and Meyer-Hofmeister, E. 2000. Evaporation: The change from accretion via a thin disk to a coronal flow. A&A, **361**(Sept.), 175–188.

Middleton, M. 2016. Black Hole Spin: Theory and Observation. Page 99 of: Bambi, C. (ed), *Astrophysics of Black Holes: From Fundamental Aspects to Latest Developments.* Astrophysics and Space Science Library, vol. 440.

Migliari, S., Tomsick, J. A., Miller-Jones, J. C. A., Heinz, S., Hynes, R. I., Fender, R. P., Gallo, E., Jonker, P. G., and Maccarone, T. J. 2010. The Complete Spectrum of the Neutron Star X-ray Binary 4U 0614+091. ApJ, **710**(Feb.), 117–124.

Miller, J. M., Tomsick, J. A., Bachetti, M., Wilkins, D., Boggs, S. E., Christensen, F. E., Craig, W. W., Fabian, A. C., Grefenstette, B. W., Hailey, C. J., Harrison, F. A., Kara, E., King, A. L., Stern, D. K., and Zhang, W. W. 2015. New Constraints on the Black Hole Low/Hard State Inner Accretion Flow with NuSTAR. ApJ, **799**(Jan.), L6.

Miniutti, G., and Fabian, A. C. 2004. A light bending model for the X-ray temporal and spectral properties of accreting black holes. MNRAS, **349**(Apr.), 1435–1448.

Mirabel, I. F., and Rodríguez, L. F. 1994. A superluminal source in the Galaxy. Nature, **371**(Sept.), 46–48.

Narayan, R., Garcia, M. R., and McClintock, J. E. 1997. Advection-dominated Accretion and Black Hole Event Horizons. ApJ, **478**(Apr.), L79–L82.

Narayan, R., Igumenshchev, I. V., and Abramowicz, M. A. 2000. Self-similar Accretion Flows with Convection. ApJ, **539**(Aug.), 798–808.

Novikov, I. D., and Thorne, K. S. 1973. Astrophysics of black holes. Pages 343–450 of: Dewitt, C., and Dewitt, B. S. (eds), *Black Holes (Les Astres Occlus)*.

O'Brien, K., Horne, K., Hynes, R. I., Chen, W., Haswell, C. A., and Still, M. D. 2002. Echoes in X-ray binaries. MNRAS, **334**(Aug.), 426–434.

Oda, H., Machida, M., Nakamura, K. E., and Matsumoto, R. 2010. Thermal Equilibria of Optically Thin, Magnetically Supported, Two-temperature, Black Hole Accretion Disks. ApJ, **712**(Mar.), 639–652.

Oda, H., Machida, M., Nakamura, K. E., Matsumoto, R., and Narayan, R. 2012. Global Structure of Optically Thin, Magnetically Supported, Two-Temperature, Black Hole Accretion Disks. PASJ, **64**(Feb.), 15.

Parker, M. L., Tomsick, J. A., Miller, J. M., Yamaoka, K., Lohfink, A., Nowak, M., Fabian, A. C., Alston, W. N., Boggs, S. E., Christensen, F. E., Craig, W. W., Fürst, F., Gandhi, P., Grefenstette, B. W., Grinberg, V., Hailey, C. J., Harrison, F. A., Kara, E., King, A. L., Stern, D., Walton, D. J., Wilms, J., and Zhang, W. W. 2015. NuSTAR and Suzaku Observations of the Hard State in Cygnus X-1: Locating the Inner Accretion Disk. ApJ, **808**(July), 9.

Patruno, A., and Watts, A. L. 2012. Accreting Millisecond X-Ray Pulsars. *ArXiv e-prints*, June.

Penrose, R. 1969. Gravitational Collapse: the Role of General Relativity. *Nuovo Cimento Rivista Serie*, **1**.

Petrucci, P. O., Merloni, A., Fabian, A., Haardt, F., and Gallo, E. 2001. The effects of a Comptonizing corona on the appearance of the reflection components in accreting black hole spectra. MNRAS, **328**(Dec.), 501–510.

Plant, D. S., Fender, R. P., Ponti, G., Muñoz-Darias, T., and Coriat, M. 2015. The truncated and evolving inner accretion disc of the black hole GX 339-4. A&A, **573**(Jan.), A120.

Ponti, G., Muñoz-Darias, T., and Fender, R. P. 2014. A connection between accretion state and Fe K absorption in an accreting neutron star: black hole-like soft-state winds? MNRAS, **444**(Oct.), 1829–1834.

Poutanen, J., and Coppi, P. S. 1998. Unification of Spectral States of Accreting Black Holes. *Physica Scripta Volume T*, **77**, 57.

Poutanen, J., and Veledina, A. 2014. Modelling Spectral and Timing Properties of Accreting Black Holes: The Hybrid Hot Flow Paradigm. Space Sci. Rev., **183**(Sept.), 61–85.

Poutanen, J., and Vurm, I. 2009. On the Origin of Spectral States in Accreting Black Holes. ApJ, **690**(Jan.), L97–L100.

Poutanen, J., Krolik, J. H., and Ryde, F. 1997. The nature of spectral transitions in accreting black holes - The case of CYG X-1. MNRAS, **292**(Nov.), L21–L25.

Qiao, E., and Liu, B. F. 2012. The Emission from an Inner Disk and a Corona in the Low and Intermediate Spectral States of Black Hole X-Ray Binaries. ApJ, **744**(Jan.), 145.

Rees, M. J. 1978. The M87 jet - Internal shocks in a plasma beam. MNRAS, **184**(Sept.), 61P–65P.

Rees, M. J., and Meszaros, P. 1994. Unsteady outflow models for cosmological gamma-ray bursts. ApJ, **430**(Aug.), L93–L96.

Remillard, R., Morgan, E., Smith, D., and Smith, E. 2000. XTE J1118+480. IAU Circ., **7389**(Mar.).

Remillard, R. A., and McClintock, J. E. 2006. X-Ray Properties of Black-Hole Binaries. ARA&A, **44**(Sept.), 49–92.

Romero, G. E., Vieyro, F. L., and Chaty, S. 2014. Coronal origin of the polarization of the high-energy emission of Cygnus X-1. A&A, **562**(Feb.), L7.

Russell, D. M., Miller-Jones, J. C. A., Maccarone, T. J., Yang, Y. J., Fender, R. P., and Lewis, F. 2011. Testing the Jet Quenching Paradigm with an Ultradeep Observation of a Steadily Soft State Black Hole. ApJ, **739**(Sept.), L19.

Rybicki, G. B., and Lightman, A. P. 1986. *Radiative Processes in Astrophysics*. Wiley-VCH.

Shakura, N. I., and Sunyaev, R. A. 1973. Black holes in binary systems. Observational appearance. A&A, **24**, 337–355.

Shapiro, S. L., and Teukolsky, S. A. 1983. *Black holes, white dwarfs, and neutron stars: The physics of compact objects*. Wiley-Interscience.

Smith, R. C. 2006. Cataclysmic variables. *Contemporary Physics*, **47**(Nov.), 363–386.

Spada, M., Ghisellini, G., Lazzati, D., and Celotti, A. 2001. Internal shocks in the jets of radio-loud quasars. MNRAS, **325**(Aug.), 1559–1570.

Stern, B. E., Poutanen, J., Svensson, R., Sikora, M., and Begelman, M. C. 1995. On the Geometry of the X-Ray–Emitting Region in Seyfert Galaxies. ApJ, **449**(Aug.), L13.

Stone, J. M., Pringle, J. E., and Begelman, M. C. 1999. Hydrodynamical non-radiative accretion flows in two dimensions. MNRAS, **310**(Dec.), 1002–1016.

Sunyaev, R. A., and Titarchuk, L. G. 1980. Comptonization of X-rays in plasma clouds - Typical radiation spectra. A&A, **86**(June), 121–138.

Tauris, T. M. 2015. Millisecond Pulsars in Close Binaries. *ArXiv e-prints*, Jan.

Tavani, M., Bulgarelli, A., Piano, G., Sabatini, S., Striani, E., Evangelista, Y., Trois, A., Pooley, G., Trushkin, S., Nizhelskij, N. A., McCollough, M., Koljonen, K. I. I., Pucella, G., Giuliani, A., Chen, A. W., Costa, E., Vittorini, V., Trifoglio, M., Gianotti, F., Argan, A., Barbiellini, G., Caraveo, P., Cattaneo, P. W., Cocco, V., Contessi, T., D'Ammando, F., Del Monte, E., de Paris, G., Di Cocco, G., di Persio, G., Donnarumma, I., Feroci, M., Ferrari, A., Fuschino, F., Galli, M., Labanti, C., Lapshov, I., Lazzarotto, F., Lipari, P., Longo, F., Mattaini, E., Marisaldi, M., Mastropietro, M., Mauri, A., Mereghetti, S., Morelli, E., Morselli, A., Pacciani, L., Pellizzoni, A., Perotti, F., Picozza, P., Pilia, M., Prest, M., Rapisarda, M., Rappoldi, A., Rossi, E., Rubini, A., Scalise, E., Soffitta, P., Vallazza, E., Vercellone, S., Zambra, A., Zanello, D., Pittori, C., Verrecchia, F., Giommi, P., Colafrancesco, S., Santolamazza, P., Antonelli, A., and Salotti, L. 2009. Extreme particle acceleration in the microquasar CygnusX-3. Nature, **462**(Dec.), 620–623.

Thompson, C., and Duncan, R. C. 1993. Neutron star dynamos and the origins of pulsar magnetism. ApJ, **408**(May), 194–217.

Uttley, P., McHardy, I. M., and Vaughan, S. 2005. Non-linear X-ray variability in X-ray binaries and active galaxies. MNRAS, **359**(May), 345–362.

Veledina, A., and Poutanen, J. 2015. Reprocessing model for the optical quasi-periodic oscillations in black hole binaries. MNRAS, **448**(Mar.), 939–945.

Veledina, A., Poutanen, J., and Vurm, I. 2011. A Synchrotron Self-Compton-Disk Reprocessing Model for Optical/X-Ray Correlation in Black Hole X-Ray Binaries. ApJ, **737**(Aug.), L17.

Veledina, A., Poutanen, J., and Ingram, A. 2013a. A Unified Lense-Thirring Precession Model for Optical and X-Ray Quasi-periodic Oscillations in Black Hole Binaries. ApJ, **778**(Dec.), 165.

Veledina, A., Poutanen, J., and Vurm, I. 2013b. Hot accretion flow in black hole binaries: a link connecting X-rays to the infrared. MNRAS, **430**(Apr.), 3196–3212.

Veledina, A., Revnivtsev, M. G., Durant, M., Gandhi, P., and Poutanen, J. 2015. Discovery of correlated optical/X-ray quasi-periodic oscillations in black hole binary SWIFT J1753.5-0127. MNRAS, **454**(Dec.), 2855–2862.

Vurm, I., and Poutanen, J. 2009. Time-Dependent Modeling of Radiative Processes in Hot Magnetized Plasmas. ApJ, **698**(June), 293–316.

Wardziński, G., and Zdziarski, A. A. 2001. Effects of non-thermal tails in Maxwellian electron distributions on synchrotron and Compton processes. MNRAS, **325**(Aug.), 963–971.

Watts, A. L. 2012. Thermonuclear Burst Oscillations. ARA&A, **50**(Sept.), 609–640.

Wijnands, R., and van der Klis, M. 1998. A millisecond pulsar in an X-ray binary system. Nature, **394**(July), 344–346.

Woods, P. M., and Thompson, C. 2006. *Soft gamma repeaters and anomalous X-ray pulsars: magnetar candidates*. Pages 547–586.

Wright, E. L., Eisenhardt, P. R. M., Mainzer, A. K., Ressler, M. E., Cutri, R. M., Jarrett, T., Kirkpatrick, J. D., Padgett, D., McMillan, R. S., Skrutskie, M., Stanford, S. A., Cohen, M., Walker, R. G., Mather, J. C., Leisawitz, D., Gautier, III, T. N., McLean, I., Benford, D., Lonsdale, C. J., Blain, A., Mendez, B., Irace, W. R., Duval, V., Liu, F., Royer, D., Heinrichsen, I., Howard, J., Shannon, M., Kendall, M., Walsh, A. L., Larsen, M., Cardon, J. G., Schick, S., Schwalm, M., Abid, M., Fabinsky, B., Naes, L., and Tsai, C.-W. 2010. The Wide-field Infrared Survey Explorer (WISE): Mission Description and Initial On-orbit Performance. AJ, **140**(Dec.), 1868–1881.

Zdziarski, A. A., Lubiński, P., and Smith, D. A. 1999. Correlation between Compton reflection and X-ray slope in Seyferts and X-ray binaries. MNRAS, **303**(Feb.), L11–L15.

Zdziarski, A. A., Pjanka, P., Sikora, M., and Stawarz, Ł. 2014. Jet contributions to the broad-band spectrum of Cyg X-1 in the hard state. MNRAS, **442**(Aug.), 3243–3255.